

Draft

Geometrical Constraints on the Hot Spot and Bipolar Outflows in Beta Lyrae

Jamie R. Lomax

*University of Denver, Department of Physics & Astronomy
2112 E. Wesley Ave, Denver, CO, 80208, USA*

Jamie.Lomax@du.edu

Jennifer L. Hoffman

*University of Denver, Department of Physics & Astronomy
2112 E. Wesley Ave, Denver, CO, 80208, USA*

Jennifer.Hoffman@du.edu

Nicholas M. Elias II

*National Radio Astronomy Observatory
Science Operations Center, PO Box O, 1003 Lopezville Road, Socorro, NM, 87801-0387,
USA*

nelias@nrao.edu

Fabienne A. Bastien¹

*Vanderbilt University, Department of Physics & Astronomy
6301 Stevenson Center, VU Station B #351807, Nashville, TN 37235*

fabienne.a.bastien@vanderbilt.edu

and

Bruce D. Holenstein

¹Fisk University, Department of Physics, 1000 17th Ave. N., Nashville, TN 37208

Gravic, Inc.

301 Lindenwood Drive Suite 100, Malvern, PA 19355-1772 USA

BHolenstein@gravic.com

ABSTRACT

We present results from six years of recalibrated and new spectropolarimetric data taken with the University of Wisconsin’s Half-Wave Spectropolarimeter (HPOL) and six years of new data taken with the photoelastic modulating polarimeter (PEMP) at the Flower and Cook Observatory. Combining these data with polarimetric data from the literature allows us to characterize the intrinsic *BVRI* polarized light curves. A repeatable discrepancy of 0.219 days (approximately 5 hours) between the secondary minima in the total light curve and the polarization curve in the *V* band, with similar behavior in the other bands, may represent the first direct evidence for an accretion hot spot on the disk edge. We also present polarization curves for several emission lines, finding evidence of eclipses suggesting the scattering region within the jets does not extend far above and below the orbital plane of the system. The line behavior at secondary eclipse also suggests the jets do not arise from the hot spot, but rather from an interior region of the disk.

Subject headings: binaries: eclipsing - stars: individual (β Lyrae) - techniques: polarimetric - accretion disks - jets

1. INTRODUCTION

Beta Lyrae A (also known as HD 174638, HR 7106 and ADS 11745A; hereafter “ β Lyr”) is a bright, well-studied semi-detached eclipsing binary star system. The primary star is a B6-B8 II, giant star (“loser”) with a mass of $3 M_{\odot}$ that is transferring matter to its main-sequence B0.5 V, $12.5 M_{\odot}$, companion (“gainer”) at about $10^{-5} M_{\odot} \text{ yr}^{-1}$ via Roche lobe overflow (Hubeny & Plavec 1991; Harmanec & Scholz 1993). This process has created a thick accretion disk that obscures the gainer (Huang 1963; Wilson 1974; Hubeny & Plavec 1991; Skulskii 1992). A bipolar flow or jet has also been detected in the system through interferometric and spectropolarimetric methods (Harmanec et al. 1996; Hoffman et al. 1998, hereafter HNF). The system’s mass ratio, q , has been placed between 4.2 and 6 with an

inclination angle, i , of 85° (Wilson 1974). Other studies have suggested $i = 83^\circ$ with $q = 5.6$ and $i = 80^\circ$ with $q = 4.28$ (Hubeny & Plavec 1991; Skulskii 1992). These large mass ratios are evidence for mass reversal in the system’s history. The disk’s ability to obscure the gainer is due to the nearly edge-on inclination angle of the system.

The system has a well-established orbital period of 12.9 days that increases at a rate of 19 s yr^{-1} (Harmanec & Scholz 1993). Recent interferometric observations have produced the first images of the system, which show the loser and the disk as separate objects and confirm the orientation of the system axis, near 254° , previously inferred from HNF’s polarimetric analysis (Zhao et al. 2008; Schmitt et al. 2009). Understanding how mass moves between and around the stars and leaves the system is imperative to understanding the evolutionary future of β Lyr. However, interferometric techniques have yet to resolve the mass stream or bipolar outflows. We have used spectropolarimetry to study the system and begin to unlock the evolutionary clues contained within the circumstellar material.

Light scattering from electrons in the highly ionized circumstellar material in β Lyr produces a variable phase-dependent polarization. Since electron scattering preserves information about the orientation of the scattering surface, analyzing polarimetric behavior as a function of wavelength allows us to determine from where in the system different spectral features have arisen. In this way, spectropolarimetric observations of β Lyr can be used to infer the geometrical properties of the scattering material in the system.

Optical polarimetry was used to study β Lyr as early as 1934, but it was not known until 1963 that the system exhibited variable polarization (Öhman 1934; Shakhovskoi 1963). Appenzeller and Hiltner (1967; hereafter AH) were the first to publish interstellar polarization (ISP) corrected broad band UBV polarization curves of β Lyr. More recently, HNF published ISP-corrected polarized light curves in the V band and $H\alpha$ and $\text{He I } \lambda 5876$ emission lines using a subset of the data we present here. HNF used the position angles of the polarized UV continuum and the hydrogen Balmer emission lines to confirm that a bipolar outflow exists in the β Lyr system after their discovery by Harmanec et al. (1996). HNF also interpreted the average position angle of the visible polarized light (164°) to be the physical axis of the binary system, an interpretation which was borne out by the interferometric images presented by Zhao et al (2008) and Schmitt et al. (2009).

In this paper we present new $BVRI$, $H\alpha$, $H\beta$, $\text{He I } \lambda 5876$, $\text{He I } \lambda 6679$, and $\text{He I } \lambda 7065$ polarization curves and polarized light curves of β Lyr. The details of our spectropolarimetric observations and our interstellar polarization corrections are in section 2. Section 3 presents and displays our observational results. We analyze our findings in section 4 and summarize conclusions in section 5.

2. OBSERVATIONS

This study compiles data from three distinct data sets. The first consists of 69 optical spectropolarimetric observations of β Lyr taken over 6 years with the University of Wisconsin’s Half-Wave Spectropolarimeter (HPOL) at the 0.9m telescope at Pine Bluff Observatory (PBO); the second data set is 3 years of archived broadband optical polarimetric data from AH taken with the 24 inch rotatable telescope at the Yerkes Observatory; and the third comprises 6 years of broadband optical polarimetric data obtained at the Flower and Cook Observatory. To calculate the phase for each observation, we used the ephemeris

$$T_{\text{pri}} = \text{JD}2,408,247.966 + 12.91378E + 3.87196 \times 10^{-6}E^2$$

where E is the total number of orbits since the primary eclipse that occurred at JD 2,408,247.966 (Harmanec & Scholz 1993). This is the same ephemeris used by HNF; it does not significantly differ from the more recent ephemeris presented by Ak et al. (2007).

2.1. HPOL Data Set

The first 14 HPOL observations, obtained between 1992 September and 1994 November, used a dual Reticon array detector with a wavelength range of 3200-7600 Å and a resolution of 15 Å (see Wolff, Nordsieck, & Nook 1996 for further instrument information). The remaining 55 observations, taken between 1995 March and 1998 September, used a CCD-based system. This extended the wavelength range, 3200-10500 Å, and increased the resolution to 7.5 Å below 6000 Å and 10 Å above (Nordsieck & Harris 1996). The first 29 observations were previously published in HNF; they have undergone recalibration for use in this study.

Table 1 lists the orbital phases along with civil and Julian dates for the midpoint of each HPOL observation. Each β Lyr observation covers the full spectral range, with the exception of the four nights indicated in Table 1. Two observations, 1995 May 27 and 1995 August 14, used only the red grating (6,000-10500 Å) of the CCD system while the other two, 1997 May 17 and 1997 May 26, used only the blue grating (3200-6000 Å).

We used 11 HPOL observations of β Lyr B taken between 1995 May and 1999 November to obtain an interstellar polarization (ISP) estimate. Beta Lyr B is a member of the same association as β Lyr A and is located 45” away (Abt et al. 1962). All of these observations were made using HPOL’s CCD-based system. Table 1 also lists the civil and Julian dates that correspond to the midpoints of each observation of β Lyr B and indicates which grating(s) were used during the observations. The first two observations, 1995 May 21 and 1996 July 3, were previously published in HNF and have undergone recalibration for this study. We

reduced all of the HPOL observations using the REDUCE software package (described by Wolff et al. 1996).

We estimated the ISP by fitting a modified Serkowski law curve to the error-weighted mean of the 11 observations of β Lyr B (Serkowski 1965; Wilking et al. 1982). The parameters for our ISP estimate are $P_{\max} = 0.422\% \pm 0.005\%$, $\lambda_{\max} = 4149 \text{ \AA} \pm 80 \text{ \AA}$, $K = 0.699$ and $PA = 151.16^\circ \pm 0.36^\circ$. We subtracted this ISP estimate from the HPOL β Lyr data. This new ISP correction has significantly improved uncertainties over previous estimates; it is consistent with the HNF estimate ($P_{\max} = 0.419\% \pm 0.013\%$, $\lambda_{\max} = 4605 \text{ \AA} \pm 260 \text{ \AA}$, and $P.A. = 151.0^\circ \pm 0.9^\circ$), which was determined using only the 1995 May 21 HPOL observation. AH found a similar estimate, $P_{\max} = 0.42\% \pm 0.04\%$ and $PA = 153.2^\circ \pm 3^\circ$ by taking the weighted mean of the observed polarization of the associated stars β Lyr B, E, and F.

2.2. AH Data Set

We also used archival BV polarization data taken between 1964 and 1966, originally published in AH. This data set consists of 37 B band and 127 V band observations, the details of which can be found in AH. We converted these data from polarization magnitudes to percent polarization for use in this study. For consistency between the HPOL and AH data sets, we did not use AH’s published ISP corrected data because included two stars (β Lyr E and F) that are not included in the HPOL ISP estimate. Instead, we subtracted only the AH UBV β Lyr B observations from their non-ISP corrected β Lyr data in each respective band.

2.3. FCO Data Set

Our last data set is made up of 19 B band, 88 V band and 17 R band observations obtained at the Flower and Cook Observatory between 1987 and 1992 with the PEMP instrument (Elias et al. 1996; Holenstein 1991). We have no observations of β Lyr B taken with the same instrument as this data set. We used the Serkowski fit to the HPOL β Lyr B observations (see Section 2.1) to calculate the ISP contributions at the central wavelengths of the BVR bands and subtracted these estimated values from the observations in this data set. We list these data and ISP subtracted data in Tables 3 through 5.

3. RESULTS

3.1. Broadband Polarimetry

To examine the behavior of the continuum polarization with orbital phase, we applied synthetic *BVRI* Johnson-Cousins band filters (described by Bessell 1990) to the ISP-corrected HPOL data. The filter routine produces the broadband values and associated internal errors for each observation; however, we must still take into account systematic variations in the instrumental polarization between nights. Systematic errors for HPOL at PBO were evaluated by periodically analyzing observations of unpolarized standard stars. Tables 6 through 9 list broadband polarization values and internal errors determined by the filter routine along with the systematic errors. In the case of the Reticon data, the systematic errors are less well determined; based on our previous experience with these data, we have estimated the uncertainties in the Stokes parameters for the Reticon data to be 0.02% in all bands. Figures 1 through 4 display these data graphically, using the larger of the internal and systematic errors for each observation.

The position angles for the *BVRI* bands remain relatively constant with orbital phase except near secondary eclipse, where the position angle values appear to rotate away from the mean value. The bottom panels in Figures 1 through 4 show this behavior in each band. In the standard picture of the system, the polarization is produced by scattering from the accretion disk edge; the average position angle at these wavelengths should therefore provide us with an estimate of the orientation of the axis of the disk and thus of the system as a whole. To calculate the average position angle in each band, we excluded the secondary eclipse points (between phases 0.425 and 0.575) because they do not follow the near-constant trend displayed at other phases and performed a linear, error-weighted, least-squares fit to the remaining data in Q - U space. We then used the slopes of the fitted lines to determine the position angles listed in Table 10. We also calculated a position angle for Balmer jump index (the vector difference between the polarization above and below the Balmer jump). As discussed in HNF, the broadband polarization in β Lyr undergoes a 90° position angle rotation across the Balmer Jump. Thus, this vector difference defines the system axis in Q - U space. Because the Balmer jump index is independent of the ISP, it provides us with an independent estimate of the orientation of the system axis.

We find the weighted mean position angle of the HPOL Reticon and CCD bands and the Balmer jump index to be $164.6^\circ \pm 0.22^\circ$. For each band, the CCD and Reticon position angles do not agree within uncertainties, with the Reticon data yielding larger position angles in all bands. This result is due to poor sampling in Q - U space; the Reticon data only consist of 14 data points in each band while there are 55 observations in the CCD V and R bands and

53 observations in the CCD B and I bands. This skews the linear fit since the full range of possible observable Q - U values is not well covered by the Reticon data. However, the larger systematic uncertainties we adopt for the Reticon data result in these points carrying a lower weight in the fit; thus, we are confident that our weighted mean is a fair representation of the true system axis. HNF found the mean V band position angle to be $163.8^\circ \pm 0.15^\circ$; while our estimate is not formally consistent with HNF's, it shows the broad band polarization behavior of the system is the same in all optical bands. Our position angle implies a system orientation of $253.8^\circ \pm 0.15^\circ$. As expected for the type of scattering in the β Lyr system, the position angle of the polarized light is perpendicular to the position angles given by Zhao et al. (2008) and Schmitt et al. (2009). Zhao et al. (2008) estimated the position angle of the system's ascending node as $253.22^\circ \pm 1.97^\circ$ and $251.87^\circ \pm 1.83^\circ$ using two different image reconstruction techniques on their interferometric data and $254.39^\circ \pm 0.83^\circ$ using a model of the system, while Schmitt et al. (2009) estimate $249.0^\circ \pm 4.0^\circ$.

We rotated all of the HPOL, AH and FCO data to the average position angle of 164° . This orients our data with respect to the intrinsic polarization axis of the system. After this rotation, $\%U$ averages to zero in each band and the polarization varies significantly only in the $\%Q$ direction. In the rest of this paper we present the projected Stokes parameter $\%Q_p$ resulting from this rotation. The use of this quantity is beneficial because it can be positive or negative, whereas $\%P$ is always positive. Points that have a position angle near 164° will have a positive $\%Q_p$ value while points with a position angle perpendicular to this (near 74°) will be negative. Hereafter we display only $\%Q_p$ because $\%U_p$ values will scatter around zero. Because the rotation is a simple trigonometric calculation, we present in Tables 6 through 9 the unrotated $\%Q$ and ISP subtracted data only.

The middle panels in Figures 1 through 4 show the $\%Q_p$ curves for the $BVRI$ bands after rotation. We used the program PERIOD04 to perform a Fourier fit to the data for each band (Lenz & Breger 2005). The PERIOD04 fitting formula is $y = Z + \sum_i^n A_i \sin(2\pi(\Omega_i t + \phi_i))$ where n is the number of sine terms in the fit, Z is the zero point, A is the amplitude, Ω is the frequency, and ϕ is the phase. The results of the fits are displayed as solid curves in each figure and their parameters are given in Table 11. The V band, and to a lesser extent the B band, Fourier fits deviate from the data at phase 0.9. This discrepancy disappears if we include three frequency terms in the Fourier fit. However, we are not as confident in the third frequency term as we are in the first two, so we only display and report parameters for the first two terms. These fits provide the first quantitative representations of the polarization variations in the β Lyr system.

The data in the $BVRI$ bands are almost always positive, indicating their position angles stay near 164° throughout the orbital period. Each of the bands displays an increase in $\%Q_p$

at primary eclipse and two other increases near the quadrature phases (0.25 and 0.75). The height difference between the polarization bumps at the quadrature phases noted by HNF disappears now that more data are added, but we note that the B and V phase 0.25 bump have a higher dispersion around the average $\%Q_p$ value than does the 0.75 phase bump. The R and I band show the opposite behavior; future observations will be able to tell us if this is due to their poor phase coverage or if the R and I are probing a different region of the disk than the B and V bands. We calculated the variance of the two quadrature bumps between phases 0.25 and 0.35, and 0.65 and 0.75 to formally show this. The first quadrature bump has $BVRI$ variances of 0.081 ± 0.006 , 0.103 ± 0.004 , 0.040 ± 0.002 , and 0.016 ± 0.002 respectively, while the second quadrature bump has variances of 0.048 ± 0.005 , 0.027 ± 0.002 , 0.281 ± 0.005 , and 0.069 ± 0.004 .

The R and I bands also produce a lower polarization signal than the B and V bands. Future observations will be able to tell us if this is a result of the lack of phase coverage in the R and I bands or if this disparity indicates scattering mechanisms other than electron scattering are present.

Each band in Figures 1 through 4 also shows that the polarization curve has a fitted minimum in polarization that occurs just prior to the secondary eclipse in total light. This minimum is accompanied by a scatter in the position angle of the polarized light away from its average value. Table 12 gives the phases of the $\%Q_P$ Fourier fit minimum in all bands. The offset between secondary eclipse in polarized light and total light is a new result, seen here for the first time due to the improved phase coverage in these data. We discuss the implications of this phenomenon in Section 4.

Figure 5 displays the projected polarized $BVRI$ flux light curves for the β Lyr system. To create these polarized light curves, we multiplied the fitted polarization curves shown in Figures 1 through 4 by their respective normalized Fourier fit light curves (Harmanec et al. 1996). In all bands, the polarized flux remains nearly constant across primary eclipse due to a decrease in total light and an increase in $\%Q_P$. The minimum near secondary eclipse seen in Figures 1 through 4 persists in Figure 5, while quadrature phases display local maxima. The B and V band appear to be the most similar; they overlap for most phases, while outside of secondary eclipse and the first quadrature phase the R and I bands produce the lowest net projected polarized flux. We do not consider the apparent height differences between bands at the quadrature phases to be significant due to the scatter in the observational points and the lack of coverage in the R and I bands.

3.2. Line Polarimetry

We also took advantage of the spectropolarimetric nature of the data by studying the polarization behavior of the strongest optical emission lines in β Lyr’s spectrum: $H\alpha$, $H\beta$, He I $\lambda 5876$, He I $\lambda 6679$, and He I $\lambda 7065$. HNF hypothesized that the $H\alpha$, $H\beta$, He I $\lambda 5876$ and He I $\lambda 7065$ lines, which show a negative projected polarization, scatter in the bipolar outflow, while the He I $\lambda 6679$ scatters on the edge of the disk. However, HNF did not have enough data to construct a full polarization phase curve for the lines. Our expanded data set allows us to do this. We present our results in graphical form only because our uncertainties are relatively large due to signal-to-noise limitations.

In order to calculate the polarization for each emission line, we used the flux equivalent width method described by HNF, using the same line and continuum regions as far as possible. We corrected the $H\alpha$ and $H\beta$ lines for underlying unpolarized absorption components (arising from the loser) in the same manner as HNF, using their preferred absorption equivalent widths of $8 \pm 2 \text{ \AA}$ for $H\alpha$ and $6 \pm 1 \text{ \AA}$ for $H\beta$. This has the following effect on the data. The continuum is positively polarized while the lines are negatively polarized. If we do not correct for unpolarized absorption, we remove too much continuum, and thus our resulting line polarization is too negative. With the absorption correction, the continuum contribution is smaller and the magnitude of the polarization is also smaller, resulting in a less negative $\%Q_p$.

We do not present the HPOL Reticon line polarization values due to their large uncertainties. Figures 6 through 10 show $\%Q_p$ and position angle curves for the $H\alpha$, $H\beta$, He I $\lambda 5876$, He I $\lambda 6697$ and He I $\lambda 7065$ lines. The $H\alpha$ (Figure 6), $H\beta$ (Figure 7), He I $\lambda 5876$ (Figure 8) and He I $\lambda 7065$ (Figure 9) lines all display a negative $\%Q_p$; thus their position angles are perpendicular to the intrinsic axis of the system. These average position angles are listed in Table 10. In addition, the polarization for each line approaches zero at both primary and secondary eclipses. For a detailed interpretation of this line behavior, see Section 4.2.

The He I $\lambda 6679$ data (Figure 10) show a polarization behavior different from that of the other lines. The data are generally positively polarized and their average position angle, 138.2° , agrees more closely with the intrinsic axis of the system than do those of the other emission lines (see Table 10). The polarization, unlike those of the other lines or the continuum bands, shows a decrease at primary eclipse but an increase at secondary eclipse. We discuss the implications of this behavior in section 4.2.

3.3. Period Analysis

Besides the primary orbital period of β Lyr (12.9 days), analysis of light curves has revealed several longer periodicities. A 340-day period was detected by Peel (1997), while both Van Hamme et al. (1995) and Harmanec et al (1996) detected a 283-day period. Wilson and Van Hamme (1999) searched polarimetry from AH, HNF, Serkowski (1965), and Shulov (1967) for periodicities but did not detect anything significant.

We performed a Lomb-Scargle power spectrum analysis to search for any periodic behavior in our polarimetric broadband (HPOL, AH, and FCO) and line data ($H\alpha$ and He I λ 5876) not associated with the 12.9 day orbital period of the system. While none of the previously detected longer periods were found, our analysis indicates the presence of periods of approximately 4.3 days in both the V and B bands with a False Alarm Probability (FAP; Horne & Baliunas 1986) of 10^{-6} when using all three data sets. None of the other bands or the line polarization data appear to contain periods other than the orbital period. We also searched for periods within the HPOL, AH and FCO data sets individually to look for any transient periodic variations. We find that the 4.3 day period also appears in the V and B AH data set with a FAP of 10^{-6} , but it does not appear in the other two data sets. This period is exactly one third of the 12.9-day orbital period of the β Lyr system and results from the combination of two separate effects: the increase in polarization at the quadrature phases due to light scattering off the disk edge and the increase in polarization at primary eclipse due to the occultation of unpolarized light by the loser (Hoffman et al. 2003, hereafter HWN). These two effects cause the $\%Q_p$ curves to form a complete cosine curve between phases 0.0 and 0.3, a second cosine curve between phases 0.3 and 0.6 and a third cosine between 0.6 and 1.0 (see Figures 1 through 4). Therefore, this period does not provide new information about the β Lyr system.

The approximately 280-day period has been ascribed to variability of the conditions of the circumstellar and circumbinary gas (Wilson 1974; Ak et al. 2007). Since polarimetric observations likely probe with this gas, in addition to the material in the disk and outflow, it follows that similar periods should appear in these data as well. However, the unevenness of our polarization observations, which are spread over days to years, requires advanced period-finding techniques. We will undertake such a study in the near future.

4. DISCUSSION

4.1. Broad Band Analysis

In interpreting their polarized flux curves, HNF proposed two different possibilities for the origin and scattering location of the visible light. In their “disk-disk” case, this light arose from within the disk and scattered from the disk edge; in the “loser-lobe” case, the V -band continuum light arose from the loser and scattered from material between the loser and the disk. In this analysis, HNF implicitly assumed that all features of the visible polarized flux curve are due to the same origin and scatterer. However, modeling work by HWN and subsequent modeling results in preparation showed that the scattered light can originate both from the loser and from the disk in differing proportions over the binary cycle. The newer results suggest the following interpretations of our $BVRI$ polarization curves. The net increase in $\%Q_p$ at primary eclipse (Figures 1-4) is the result of the unpolarized light from the primary star being blocked by the disk material at phase 0.0. HNF interpreted the increase in $\%Q_p$ at the quadrature phases as arising in one of two ways: light originating from within the disk and scattering from the disk edge, or light originating from the loser and scattering from material between the stars. Subsequent modeling work by Hoffman suggests that these “quadrature bumps” can form simply by loser light scattering from the disk edge. The minimum at secondary eclipse occurs because the unpolarized primary star blocks light scattered in the secondary component.

Near secondary eclipse in all four broadband $\%Q_p$ curves, the minimum in polarization precedes the minimum in total light; the phases for the polarization minimum in the $BVRI$ bands are listed in Table 12. In each band, this minimum corresponds to a rotation in position angle away from the average value; the phase ranges for this rotation are also listed in Table 4. In the basic star-star-disk model for the system, there is no mechanism to produce this disparity. If the loser is an unpolarized source, as indicated by the absence of a primary eclipse in the polarized flux curves (Figure 5; HNF), then the polarization minimum produced by its transit across the disk should be centered at flux minimum (phase 0.5; HWN). Thus, to explain this offset, we need to invoke another system component. Since β Lyr is a mass transfer system, it most likely contains a mass stream connecting the loser and the disk as well as a ‘hot spot’ where the mass stream from the loser impacts the disk edge (Lubow & Shu 1975, see also the geometries proposed by HNF). A hot spot could potentially decrease observed polarization from the disk edge by disrupting the otherwise smooth structure of the disk edge and adding unpolarized light at phases when it is visible. On the other hand, a mass stream would tend to have a similar position to that of the disk and would not show up as a decrease in the observed polarization. The effects of a hot spot would be detectable in the polarization light curves in the $BVRI$ bands because the

disk is the primary scattering region for visible light in the β Lyr system. But, if it is not significantly brighter than the surrounding disk, the hot spot would not be visible in the total light curves. Therefore, we interpret the $\%Q_P$ minimum associated with the randomization of the polarized position angle prior to secondary eclipse as the first direct evidence for the proposed hot spot on the β Lyr disk edge (Lubow & Shu 1975; Harmanec 2002).

We expect the hot spot to create an unstructured region on the disk edge where the polarization vectors of the scattered light are randomized in position angle. When this part of the disk is visible, the hot spot should cause a decreased polarization signal and a rotation in position angle, both of which occur in our polarization curves (Figures 1-4). As long as the hot spot does not lie on the line connecting the centers of mass of the two stars, and its brightness in the visible continuum is similar to that of the undisturbed disk, its effect should result in a minimum in polarization that does not correspond to a minimum in flux. Hydrodynamical modeling of the β Lyr system indicates that the mass stream, and therefore its associated hot spot, should lead the loser in the sense of rotation of the system (Nazarenko & Glazunova 2006; Lubow & Shu 1975). In the β Lyr polarization curves, the polarization minimum and concurrent position angle variation occur just before secondary eclipse, suggesting that the hot spot begins its transit of the disk before the loser does. In fact, the larger dispersion of points in the B and V bands at the first quadrature phase when compared to the second quadrature phase is an indication that the hot spot is already in view by phase 0.25. The minimum polarization occurs at the phases where the disk area disrupted by the hot spot and eclipsed by the loser is maximized. We sketch this proposed interpretation in Figure 11.

We note that there are less data points post-secondary eclipse in all bands which may skew the $\%Q_P$ Fourier fit near secondary minimum. However, we have several reasons to believe this is not the case. The $\%Q_P$ near secondary minimum effect is apparent in all filters; some of which have a much lower point density in phase than the V band. However, the V band displays the smallest difference between the $\%Q_P$ near secondary minimum and phase 0.5. The position angle rotation does not heavily depend on the number of points, is apparent in all bands and has a larger effect at pre-secondary eclipse phases. Finally, the uncertainties on the phases at which the minima occur are small (see Table 12) compared to the difference between phase 0.5 and the polarization secondary minimum. Future work will include filling in the post-secondary data gap with new HPOL observations to improve the Fourier fits and quantify the $\%Q_P$ near secondary minimum offsets more reliably.

In the subsections below, we outline three different estimates of the size of the hot spot, assuming it has the same height as the edge of the disk. We use the following values for system parameters: a loser radius of $R_L = 8.5R_\odot$, a disk diameter of $D_D = 60R_\odot$, a system

radius of $R_S = 58R_\odot$ and a disk height of $H_D = 16R_\odot$ (Linnell 2000).

4.1.1. Hot Spot Size Estimate: % Q_P Method

We can use the offset in secondary eclipse to estimate a maximum size for the hot spot. Assuming circular orbits, we have the scenario depicted in Figure 12. Knowing that phase 0.5 occurs at an angle of 180° on the circle depicting the loser’s orbit, we can use a simple ratio to find the angle θ ,

$$\frac{0.5}{180^\circ} = \frac{P}{180^\circ - \theta} \quad (1)$$

where P is the phase for which secondary eclipse occurs in polarized light (Table 12) and $180^\circ - \theta$ is the angle from zero at which phase P occurs. If we know θ , we can also find the length of line x ,

$$x = R_S \sin(\theta) \quad (2)$$

where R_S is the radius between the center of the disk and the center of the loser. When the length of line x is larger than the radius of the loser, R_L , we have the following equation for the projected size of the hot spot, HS_Q ,

$$HS_Q = \begin{cases} 60R_\odot & \text{for } x \geq \frac{1}{2}D_D, \\ (x - R_L) + \frac{1}{2}D_D & \text{for } \frac{1}{2}D_D > x > R_L, \\ \frac{1}{2}D_D - (R_L - x) & \text{for } R_L > x > 0 \end{cases} \quad (3)$$

where D_D is the diameter of the accretion disk.

Using the above formulae we can calculate the maximum projected hot spot size for the *BVRI* bands. Table 4 lists the results. The maximum hot spot size ranges from $28R_\odot$ to $40R_\odot$. Since we assume the hot spot has the same height as the disk, these values represent ‘widths’ along the projected face of the disk. We do not calculate formal error bars on these estimates because they vary so widely.

4.1.2. Hot Spot Size Estimate: Position Angle Method

We also used the variations in position angle to calculate a maximum size for the hot spot. First, we calculated the size of the disk in phase. To do this we solved Equation 2 for θ when $x = \frac{1}{2}D_D$. The phase for the left side of the disk as depicted in Figure 12 is then given by Equation 1. We calculate this phase to be 0.413. Similarly for the right side of the disk we calculate a phase of 0.587. The resulting size of the disk in phase is the difference of these phases, or 0.174.

We then estimated the size of the hot spot in phase by finding how long the randomization of position angle lasts. We assumed any points near secondary eclipse that deviated from the average position angle were due to the hot spot. We do not use a formal calculation to find these points; we choose the smallest and largest phases for the randomized position angles by eye. We then took the difference in phase between the deviant observations with the smallest and largest phases to calculate the size of the hot spot in phase, θ_{HS} (Table 12). The maximum hot spot size, HS_{PA} , is given by the ratio

$$\frac{60R_{\odot}}{0.174} = \frac{HS_{PA}}{\theta_{HS}}. \quad (4)$$

Table 12 lists the maximum projected size of the hot spot across the edge of the disk for each band. Our hot spot size estimates found with this method range from $26R_{\odot}$ to $55R_{\odot}$.

4.1.3. Hot Spot Size Estimate: Simple Model

We used a simple model for a third estimate of the size of the hot spot. For this model we assume the polarization of the disk is uniform across the disk edge. We first calculated a baseline qf_{DC} , the polarized flux due to the disk’s self-illumination, by taking the error-weighted mean $\%Q_P$ multiplied by the normalized Fourier fit of the observations between phases 0.7 and 1.2 for each band (HWN). This assumes all the polarized flux at these phases is due to light originating within the disk rather than from the loser, a reasonable assumption given the results of HWN. We also define qf_{min} , the minimum polarized flux near secondary eclipse due to the primary star’s eclipse and hot spot’s transit of the disk, to be the error-weighted mean $\%Q_P$ multiplied by the normalized Fourier fit for observations between phases 0.4 and 0.55. If we subtract from qf_{DC} the amount of polarized flux blocked by the primary star and disrupted by the transit of the hot spot, the result should be qf_{min} , the polarized flux observed at secondary eclipse.

The amount of polarized flux lost due to the primary eclipsing the disk and the hot spot transiting the disk is given by

$$qf_{DC} - \frac{qf_{DC}}{A_D} A_{ecl} - \frac{qf_{DC}}{A_D} A_{HS} = qf_{min} \quad (5)$$

where A_{ecl} is the area of the disk eclipsed by the primary star (shaded region in Figure 12), A_D is the observed area of the edge of the disk, and $A_{HS} = H_D HS_{SM}$ is the area of the disk edge disrupted by the hot spot. The fraction $q_{DC}/A_D = q_{DC}/D_D H_D$ gives the polarized flux per unit area from the disk. The second term in Equation 5 is the polarized flux eclipsed by the primary star and the third term is the polarized flux subtracted by the hot spot. Table 12 gives qf_{DC} and the resulting hot spot size estimate for the *BVRI* bands.

Comparing all three methods, we find a wide range of sizes for the hot spot. The smallest size estimate is $17R_{\odot}$ while the largest is $55R_{\odot}$. The only estimate method that produces a different size for the R and I bands is the simple model. With more data it is likely that other two methods would produce different size estimates; however, the polarimetric behavior of the system in the R and I bands is very similar (see Figure 5). The B band estimates have the closest agreement between the three methods; they range from $28R_{\odot}$ to $36R_{\odot}$, while the V band estimates have the largest range, $24R_{\odot}$ to $55R_{\odot}$. The overlap region for size ranges in all the bands is $28R_{\odot}$ to $40R_{\odot}$; this range is likely an upper limit for the size of the hot spot. The large size of our estimates may indicate that we are actually detecting the mass stream and not a hot spot. However, this scenario would not likely produce the phenomena seen in Figures 1 through 4 because the mass stream would tend to have a position angle similar to that of the disk; therefore, we prefer a large hot spot interpretation.

4.2. Line Analysis

The polarization curves of the $H\alpha$, $H\beta$, He I $\lambda 5876$, and He I $\lambda 7065$ lines all show eclipse effects. Although all the lines we studied are polarized at some phases of the binary cycle, at primary and secondary eclipse the polarization of each line is near zero. For this to happen, the scattering region for these lines must lie near enough to the orbital plane of the system to be occulted both by the loser and by the disk. HNF previously suggested that these lines scatter in the bipolar outflows because their average position angles lie near 74° , corresponding to negative values of $\%Q_P$. The results from our extended data set support this interpretation and further suggest that the scattering region within the outflows must lie between the loser and the disk and have a vertical extent comparable to the height of the disk.

We also note that the polarization curves of these five lines show no evidence of a polarization minimum offset at secondary eclipse, as do the broadband curves. Given the large uncertainties in the line polarization measurements, this is not a robust conclusion; however, if confirmed by further observations, the lack of an offset would suggest that the outflows do not originate at the hot spot (as suggested by Harmenec et al. 2002). If this were the case, the secondary minimum in the line polarization curves should occur after the secondary eclipse in total light, since the hot spot leads the loser. Further, the outflows cannot be centered on the gainer as assumed by HNF, since in this case the line polarization would show no primary eclipse. Our results imply a third possibility: that the jets are located along the line of centers between the two stars in the β Lyr system. They may originate near the surface of the gainer, forming as disk material accretes onto the invisible star; this

scenario is similar to that assumed by HNF, but it requires that the jets be confined to a localized region near the gainer’s surface on the side facing the loser. However, the large uncertainties and scatter in Figures 5 through 8 make it difficult to pinpoint a location for the origin of the jets with confidence. Higher-precision line polarization measurements will clarify the situation by helping to distinguish between model scenarios.

The He I $\lambda 6679$ line (Figure 10) displays a much different polarimetric behavior than the other lines; its projected polarization is positive, indicating a position angle aligned with that of the broadband continuum, and increases at secondary eclipse instead of approaching zero as does that of the other lines. HNF pointed out that the He I $\lambda 6679$ line is not collisionally excited and must therefore arise in hot nebular gas, such as in the mass stream; they suggest that it then scatters from the mass stream and the accretion disk edge.

The polarization curve of the He I $\lambda 6679$ line is not consistent with the interpretation that it scatters in the mass stream. The mass stream should be eclipsed by the loser and disk approximately between phases 0.5 and 1.2 as it goes around the back of the disk; however, the He I $\lambda 6679$ polarization increases at secondary eclipse. This suggests that at secondary eclipse, either the scatterer is in full view, the source of unpolarized light is blocked, or both. The position angle values are consistent with scattering in the disk, which is only partially eclipsed at phase 0.5. The jets are the only other system component eclipsed at this phase, suggesting that the He I $\lambda 6679$ line forms in the hot nebular gas in the jet, in the region that stays close to the plane and scatters the $H\alpha$, $H\beta$, He I $\lambda 5876$, and He I $\lambda 7065$ lines and then scatters in the disk.

5. SUMMARY

We have presented a large new data set of polarimetric observations of β Lyr in the *BVRI* bands and the first Fourier fits to the polarimetric variations in these bands and several emission lines. We have interpreted the minimum in the *BVRI* projected polarization prior to secondary eclipse and the associated position angle rotations as the first direct evidence for a hot spot on the edge of the accretion disk in the β Lyr system. Using the phases of polarization minimum, the scatter of the position angle and a simple model, we have estimated the size of the hot spot to be between 17 and 55 R_{\odot} across the face of the disk.

We expect the hot spot may also be detectable in X-rays. Both ROSAT HRI (Berghofer & Schmitt 1994) and Suzaku (Ignace et al. 2008) have detected strong and variable X-ray emission from β Lyr. However, neither set of observations has provided information on the origin of the X-ray emission or observed the system at phases which we see the hot spot

effects. An X-ray light curve with more complete phase coverage will help locate the source of the X-ray emission.

The presence of both primary and secondary eclipses in the polarization curves of emission lines of $H\alpha$, $H\beta$ and two helium lines, which we hypothesize scatter in the bipolar outflows in the system, indicate that the outflows do not originate at the hot spot. They likely arise from a source located somewhere between the centers of the two stars. Further high-precision line polarimetry will place more restrictive constraints on the location of the jets.

Advancements in technology will soon allow for the combination of long-baseline optical interferometry with polarimetry (Elias et al. 2008). We expect such a technological development will provide new and exciting geometrical insights into the β Lyr system and others like it.

We are very grateful to Brian Babler, Marilyn Meade, and Ken Nordsieck for their help with the HPOL data and to all of the members of the PBO science team for their help in obtaining the HPOL data used in this paper. We are indebted to the late R.H. Koch for his observing efforts at FCO and to his wife Joanne for allowing us to use those data. We also thank Keivan Stassun for his help with the period analysis and Petr Harmanec for providing us with unpolarized *UBVRI* light curves of β Lyr. We have had useful conversations with many colleagues: Kathleen Geise, Paul Hemenway, K. Tabetta Hole, Richard Ignace, Brian Kloppenborg, Robert Stencel, and Toshiya Ueta. JRL acknowledges support through the NASA Harriett G. Jenkins Pre-doctoral Fellowship Program and Sigma Xi’s Grants-in-Aid of Research program. JLH acknowledges support through NASA ADP award NNH08CD10C and NSF award AST-0807477. FAB acknowledges support from NSF grant AST-0849736 (K. Stassun, PI) and from a GAANN Fellowship.

REFERENCES

- Abt, H. A., Jeffers, H. M., Gibson, J., & Sandage, A. R. 1962, *ApJ*, 135, 429
- Ak, H., et al. 2007, *A&A*, 463, 233
- Appenzeller, I., & Hiltner, W. A. 1967, *ApJ*, 149, 353
- Elias, N. M., II, Koch, R. H., & Holenstein, B. D. 1996, *BAAS*, 28, 913
- Elias, N. M., II, Jones, C. E., Schmitt, H. R., Jorgensen, A. M., Ireland, M. J., & Perraut, K. 2008, arXiv:0811.3139

- Harmanec, P. 2002, *Astronomische Nachrichten*, 323, 87
- Harmanec, P., et al. 1996, *A&A*, 312, 879
- Harmanec, P., & Scholz, G. 1993, *A&A*, 279, 131
- Holenstein, B. D. 1991, Ph.D. Thesis
- Hoffman, J. L., Nordsieck, K. H., & Fox, G. K. 1998, *AJ*, 115, 1576
- Hoffman, J. L., Whitney, B. A., & Nordsieck, K. H. 2003, *ApJ*, 598, 572
- Horne, J. H., & Baliunas, S. L. 1986, *ApJ*, 302, 757
- Huang, S.-S. 1963, *ApJ*, 138, 342
- Hubeny, I., & Plavec, M. J. 1991, *AJ*, 102, 1156
- Lubow, S. H., & Shu, F. H. 1975, *ApJ*, 198, 383
- Lenz, P., & Breger, M. 2005, *Communications in Asteroseismology*, 146, 53
- Linnell, A. P. 2000, *MNRAS*, 319, 255
- Nazarenko, V. V., & Glazunova, L. V. 2006, *Astronomy Reports*, 50, 369
- Nordsieck, K. H., & Harris, W. 1996, *Polarimetry of the Interstellar Medium*, 97, 100
- Öhman, Y. 1934, *Nature*, 134, 534
- Peel, M. 1997, *MNRAS*, 284, 148
- Schmitt, H. R., et al. 2009, *ApJ*, 691, 984
- Serkowski, K. 1965, *ApJ*, 142, 793
- Shakhovskoi, N. M. 1963, *Soviet Astronomy*, 6, 587
- Shulov, O. S. 1967, *Proc. Astr. Obs. Leningrad Univ.*, 24, 38
- Skulskii, M. Y. 1992, *Soviet Ast.Letters*, 18, 287
- Wiling, B. A., Lebofsky, M. J., & Rieke, G. H. 1982, *AJ*, 87, 695
- Wilson, R. E. 1974, *ApJ*, 189, 319
- Wilson, R. E., & van Hamme, W. 1999, *MNRAS*, 303, 736

Wolff, M. J., Nordsieck, K. H., & Nook, M. A. 1996, *AJ*, 111, 856

Zhao, M., et al. 2008, *ApJ*, 684, L95

Table 1. Date and Phase Information for Midpoints of the HPOL β Lyrae and β Lyrae B Observations

Date	JD - 2,400,000	Phase ^a
β Lyr Reticon (through HNF; recalibrated):		
1992 Sep 30	48895.71	0.661
1992 Oct 6	48901.67	0.121
1992 Oct 13	48908.60	0.657
1992 Oct 27	48922.58	0.737
1992 Dec 28	48984.52	0.525
1993 Jul 26	49194.60	0.762
1994 Jun 3	49506.78	0.890
1994 Jun 30	49533.59	0.962
1994 Jul 22	49555.66	0.668
1994 Jul 29	49562.62	0.206
1994 Jul 31	49564.59	0.358
1994 Sep 8	49603.53	0.368
1994 Sep 20	49615.49	0.292
1994 Nov 7	49663.46	0.000
β Lyr CCD (through HNF, recalibrated):		
1995 Mar 14 ^b	49790.89	0.848
1995 May 5	49842.82	0.862
1995 May 26	49863.82	0.485
1995 May 27 ^c	49864.78	0.559
1995 May 30	49867.84	0.796
1995 Jun 4	49872.86	0.184
1995 Jul 3	49901.66	0.410
1995 Jul 10	49908.72	0.955
1995 Jul 12	49910.82	0.117
1995 Jul 18	49916.70	0.572
1995 Jul 24	49922.79	0.043
1995 Aug 6	49935.68	0.039
1995 Aug 14 ^c	49943.63	0.653
1995 Aug 18	49947.72	0.969
1995 Sep 10	49970.74	0.749

Table 1—Continued

Date	JD - 2,400,000	Phase ^a
<i>β</i> Lyr CCD (after HNF, final calibration):		
1996 Aug 21	50316.65	0.483
1997 May 17 ^d	50585.78	0.283
1997 May 26 ^d	50594.80	0.980
1997 Jul 5	50634.82	0.073
1997 Jul 7	50636.72	0.219
1997 Jul 7	50636.80	0.226
1997 Jul 10	50639.67	0.447
1997 Jul 10	50639.77	0.455
1997 Jul 10	50639.87	0.463
1997 Jul 11	50640.68	0.525
1997 Jul 11	50640.79	0.534
1997 Jul 15	50644.66	0.833
1997 Jul 15	50644.77	0.842
1997 Jul 15	50644.86	0.848
1997 Jul 16	50645.68	0.912
1997 Jul 16	50645.78	0.920
1997 Jul 18	50647.71	0.069
1997 Aug 1	50661.64	0.145
1997 Aug 25	50685.64	0.000
1997 Aug 25	50685.74	0.008
1997 Aug 25	50685.83	0.015
1997 Aug 26	50686.66	0.079
1997 Aug 30	50690.62	0.385
1997 Sep 7	50698.63	0.004
1997 Sep 7	50698.71	0.010
1997 Sep 12	50703.77	0.401
1997 Sep 21	50712.64	0.087
1997 Sep 25	50716.73	0.403
1997 Oct 3	50724.60	0.011
1997 Oct 3	50724.70	0.019

Table 1—Continued

Date	JD - 2,400,000	Phase ^a
1997 Oct 4	50725.57	0.086
1997 Oct 28	50749.54	0.939
1997 Nov 17	50769.56	0.486
1997 Dec 15	50797.50	0.645
1998 Apr 19	50922.86	0.333
1998 Apr 24	50927.90	0.723
1998 Jun 23	50987.82	0.354
1998 Jul 31	51025.78	0.287
1998 Aug 31	51056.62	0.671
1998 Sep 8	51064.76	0.300
<i>β</i> Lyr B CCD (through HNF, recalibrated):		
1995 May 21	49858.85	...
1996 Jul 3	50267.75	...
<i>β</i> Lyr B CCD (after HNF, final calibration):		
1998 Dec 8 ^c	51155.54	...
1998 Dec 11 ^c	51158.53	...
1998 Dec 12 ^d	51159.52	...
1999 Aug 30	51420.63	...
1999 Sep 13	51434.64	...
1999 Oct 3 ^d	51454.59	...
1999 Nov 1 ^d	51483.60	...
1999 Nov 2	51484.57	...
1999 Nov 15 ^d	51497.55	...

^aPhases were calculated using the ephemeris in Harmanec & Scholz (1993).

^bTable 1 of HNF incorrectly lists this date as 1994 March 14.

^cThese observations used only the red grat-

ing; see Section 2.1.

^dThese observations used only the blue grating; see Section 2.1.

Table 2. Date and Phase Information for Midpoints of the FCO β Lyrae Observations

Date	JD - 2,400,000	Phase ^a
<i>B</i> Band:		
1989 Apr 12	47628.88	0.753
1989 Apr 20	47636.85	0.352
1989 Apr 23	47639.85	0.583
1989 May 29	47675.80	0.366
1989 Jun 5	47682.78	0.907
1989 Jun 12	47689.80	0.448
1989 Jun 19	47696.78	0.989
1989 Jun 30	47707.76	0.840
1989 Jul 2	47709.79	0.994
1989 Jul 25	47732.74	0.772
1989 Jul 29	47736.79	0.081
1989 Aug 31	47769.68	0.632
1989 Sep 3	47772.58	0.844
1989 Sep 4	47773.57	0.922
1989 Sep 5	47774.57	0.999
1989 Sep 9	47778.57	0.308
1989 Oct 5	47804.45	0.318
1989 Oct 8	47807.60	0.550
1992 Jun 4	48777.76	0.543
<i>V</i> Band:		
1987 Aug 11	47018.61	0.563
1987 Aug 13	47020.57	0.718
1987 Aug 15	47022.59	0.872
1987 Aug 16	47023.58	0.949
1987 Aug 18	47025.54	0.104
1987 Aug 18	47025.56	0.104
1987 Aug 20	47027.59	0.259
1987 Aug 21	47028.58	0.336
1987 Aug 22	47029.56	0.413
1987 Aug 24	47031.58	0.568

Table 2—Continued

Date	JD - 2,400,000	Phase ^a
1987 Sep 15	47053.57	0.268
1987 Sep 26	47064.55	0.119
1987 Sep 27	47065.54	0.196
1987 Sep 28	47066.55	0.273
1987 Oct 5	47073.55	0.814
1987 Oct 6	47074.53	0.892
1988 Jun 13	47325.80	0.313
1988 Jun 24	47336.80	0.163
1988 Jun 28	47340.61	0.453
1988 Jul 1	47343.62	0.685
1988 Jul 16	47358.66	0.863
1988 Aug 19	47392.69	0.491
1988 Aug 22	47395.68	0.723
1988 Aug 23	47396.59	0.781
1988 Sep 1	47405.62	0.477
1988 Sep 2	47406.58	0.554
1988 Sep 3	47407.59	0.631
1988 Sep 7	47411.56	0.941
1988 Sep 8	47412.55	0.018
1988 Sep 11	47415.55	0.250
1988 Sep 15	47419.55	0.559
1988 Sep 16	47420.55	0.636
1988 Sep 27	47431.54	0.487
1988 Sep 28	47432.50	0.564
1988 Sep 29	47433.53	0.641
1988 Oct 1	47435.57	0.796
1988 Oct 2	47436.54	0.873
1988 Oct 6	47440.56	0.182
1988 Oct 10	47444.52	0.491
1988 Oct 14	47448.52	0.801
1988 Oct 15	47449.57	0.878

Table 2—Continued

Date	JD - 2,400,000	Phase ^a
1988 Oct 26	47460.47	0.728
1988 Oct 27	47461.57	0.805
1988 Oct 28	47462.53	0.883
1988 Oct 30	47464.50	0.037
1988 Oct 31	47465.49	0.115
1988 Nov 4	47469.50	0.424
1988 Nov 10	47475.53	0.888
1988 Nov 14	47479.50	0.197
1988 Nov 15	47480.47	0.274
1988 Nov 18	47483.49	0.506
1989 Apr 12	47628.85	0.733
1989 Apr 20	47636.83	0.352
1989 Apr 23	47639.83	0.583
1989 May 29	47675.78	0.366
1989 Jun 5	47682.80	0.907
1989 Jun 12	47689.82	0.448
1989 Jun 19	47696.80	0.989
1989 Jun 30	47707.78	0.840
1989 Jul 2	47709.81	0.994
1989 Jul 25	47732.76	0.772
1989 Jul 29	47736.82	0.081
1989 Aug 31	47769.70	0.632
1989 Sep 3	47772.60	0.844
1989 Sep 4	47773.61	0.922
1989 Sep 5	47774.60	0.999
1989 Sep 9	47778.60	0.308
1989 Oct 2	47801.68	0.105
1989 Oct 23	47822.59	0.709
1992 Jun 13	48786.72	0.239
1992 Jun 18	48791.65	0.625
1992 Jun 21	48794.62	0.838

Table 2—Continued

Date	JD - 2,400,000	Phase ^a
1992 Jun 28	48801.73	0.398
1992 Jun 29	48802.67	0.476
1992 Jul 6	48809.68	0.017
1992 Jul 8	48811.59	0.152
1992 Jul 19	48822.60	0.002
1992 Jul 29	48832.57	0.775
1992 Jul 30	48833.58	0.852
1992 Aug 2	48836.61	0.084
1992 Aug 3	48837.60	0.161
1992 Aug 5	48839.60	0.316
1992 Aug 8	48842.56	0.548
1992 Aug 11	48845.56	0.780
1992 Aug 19	48853.54	0.398
1992 Aug 30	48864.56	0.248
1992 Sep 1	48866.60	0.403
1992 Sep 13	48878.55	0.330
<i>R</i> Band:		
1989 Apr 12	47628.90	0.753
1989 Apr 20	47636.81	0.352
1989 Apr 23	47639.79	0.583
1989 May 29	47675.76	0.366
1989 Jun 5	47682.83	0.907
1989 Jun 12	47689.84	0.448
1989 Jun 19	47696.82	0.989
1989 Jun 30	47707.80	0.840
1989 Jul 2	47709.83	0.994
1989 Jul 25	47732.78	0.772
1989 Jul 29	47736.84	0.081
1989 Aug 31	47769.72	0.632
1989 Sep 3	47772.62	0.844
1989 Sep 5	47774.62	0.999

Table 2—Continued

Date	JD - 2,400,000	Phase ^a
1989 Sep 9	47778.62	0.308
1989 Oct 2	47801.65	0.105
1989 Oct 10	47809.61	0.704

Table 3. FCO *B* Filter Data

Phase	% <i>Q</i>	% <i>U</i>	ISP sub % <i>Q</i>	ISP sub % <i>U</i>	Internal Error % <i>Q</i>	Internal Error % <i>U</i>
0.081	0.395	-0.432	0.164	-0.067	0.007	0.007
0.308	0.579	-0.493	0.348	-0.128	0.016	0.014
0.318	0.617	-0.527	0.386	-0.162	0.010	0.008
0.352	0.405	-0.438	0.174	-0.073	0.008	0.008
0.366	0.549	-0.520	0.318	-0.155	0.009	0.008
0.448	0.257	-0.261	0.026	0.104	0.007	0.007
0.543	0.148	-0.350	-0.083	0.015	0.009	0.009
0.550	0.460	-0.698	0.229	-0.333	0.016	0.023
0.583	0.421	-0.527	0.190	-0.162	0.008	0.010
0.632	0.497	-0.517	0.266	-0.152	0.010	0.010
0.753	0.538	-0.479	0.307	-0.114	0.014	0.012
0.772	0.486	-0.494	0.255	-0.129	0.011	0.011
0.840	0.416	-0.469	0.185	-0.104	0.007	0.008
0.844	0.406	-0.476	0.175	-0.111	0.009	0.011
0.907	0.531	-0.488	0.300	-0.123	0.012	0.011
0.922	0.470	-0.456	0.239	-0.091	0.010	0.010
0.989	0.602	-0.566	0.371	-0.201	0.010	0.010
0.994	0.635	-0.558	0.404	-0.193	0.018	0.016
0.999	0.553	-0.645	0.322	-0.280	0.009	0.010

Table 4. FCO V Filter Data

Phase	% Q	% U	ISP sub % Q	ISP sub % U	Internal Error % Q	Internal Error % U
0.002	0.353	-0.393	0.134	-0.028	0.053	0.053
0.017	0.405	-0.471	0.186	-0.106	0.013	0.013
0.018	0.508	-0.433	0.289	-0.068	0.010	0.009
0.037	0.687	-0.704	0.468	-0.339	0.097	0.099
0.081	0.390	-0.422	0.171	-0.057	0.010	0.011
0.084	0.390	-0.423	0.171	-0.058	0.010	0.010
0.104	0.287	-0.412	0.068	-0.047	0.014	0.019
0.104	0.292	-0.437	0.073	-0.072	0.008	0.012
0.105	0.548	-0.458	0.329	-0.093	0.010	0.009
0.115	0.310	-0.418	0.091	-0.053	0.006	0.008
0.119	0.335	-0.454	0.116	-0.089	0.008	0.011
0.152	0.440	-0.416	0.221	-0.051	0.012	0.012
0.161	0.442	-0.438	0.223	-0.073	0.010	0.010
0.163	0.370	-0.390	0.151	-0.025	0.092	0.096
0.182	0.519	-0.431	0.300	-0.066	0.012	0.010
0.196	0.397	-0.457	0.178	-0.092	0.009	0.010
0.197	0.451	-0.474	0.232	-0.109	0.015	0.016
0.239	0.322	-0.454	0.103	-0.089	0.015	0.015
0.248	0.500	-0.510	0.281	-0.145	0.006	0.006
0.250	0.492	-0.466	0.273	-0.101	0.014	0.013
0.259	0.412	-0.441	0.193	-0.076	0.009	0.010
0.268	0.420	-0.433	0.201	-0.068	0.007	0.007
0.273	0.493	-0.448	0.274	-0.083	0.008	0.008
0.274	0.549	-0.570	0.330	-0.205	0.011	0.011
0.308	0.560	-0.461	0.341	-0.096	0.013	0.011
0.313	0.408	-0.419	0.189	-0.054	0.009	0.009
0.316	0.526	-0.492	0.307	-0.127	0.008	0.008
0.330	0.580	-0.475	0.361	-0.110	0.012	0.012
0.336	0.461	-0.423	0.242	-0.058	0.008	0.008
0.352	0.391	-0.421	0.172	-0.056	0.008	0.009
0.366	0.556	-0.495	0.337	-0.130	0.012	0.011
0.398	0.455	-0.428	0.236	-0.063	0.021	0.021
0.398	0.332	-0.397	0.113	-0.032	0.012	0.012
0.403	0.492	-0.401	0.273	-0.036	0.009	0.009
0.413	0.312	-0.268	0.093	0.097	0.044	0.039
0.424	0.405	-0.414	0.186	-0.049	0.008	0.008
0.448	0.269	-0.273	0.050	0.092	0.007	0.007
0.453	0.318	-0.282	0.099	0.083	0.009	0.008
0.476	0.233	-0.198	0.014	0.167	0.017	0.017
0.477	0.328	-0.268	0.109	0.097	0.006	0.005
0.487	0.430	-0.413	0.211	-0.048	0.008	0.007
0.491	0.281	-0.349	0.062	0.016	0.009	0.011
0.491	0.434	-0.432	0.215	-0.067	0.013	0.010
0.506	0.501	-0.401	0.282	-0.036	0.011	0.009
0.548	0.316	-0.455	0.097	-0.090	0.019	0.019
0.554	0.354	-0.345	0.135	0.020	0.010	0.009

Table 4—Continued

Phase	% Q	% U	ISP sub % Q	ISP sub % U	Internal Error % Q	Internal Error % U
0.559	0.341	-0.468	0.122	-0.103	0.007	0.009
0.563	0.355	-0.389	0.136	-0.024	0.007	0.008
0.564	0.372	-0.445	0.153	-0.080	0.013	0.016
0.568	0.322	-0.402	0.103	-0.037	0.006	0.008
0.583	0.421	-0.501	0.202	-0.136	0.013	0.015
0.625	0.517	-0.523	0.298	-0.158	0.004	0.004
0.631	0.514	-0.438	0.295	-0.073	0.011	0.009
0.632	0.475	-0.469	0.256	-0.104	0.012	0.011
0.636	0.328	-0.247	0.109	0.118	0.009	0.007
0.641	0.575	-0.390	0.356	-0.025	0.013	0.010
0.685	0.507	-0.438	0.288	-0.073	0.010	0.009
0.709	0.508	-0.488	0.289	-0.123	0.009	0.008
0.718	0.521	-0.398	0.302	-0.033	0.012	0.010
0.723	0.558	-0.473	0.339	-0.108	0.011	0.009
0.728	0.478	-0.470	0.259	-0.105	0.009	0.009
0.733	0.518	-0.459	0.299	-0.094	0.009	0.008
0.772	0.480	-0.449	0.261	-0.084	0.011	0.010
0.775	0.508	-0.491	0.289	-0.126	0.011	0.011
0.780	0.458	-0.477	0.239	-0.112	0.010	0.010
0.781	0.483	-0.419	0.264	-0.054	0.010	0.009
0.796	0.462	-0.417	0.243	-0.052	0.010	0.009
0.801	0.422	-0.446	0.203	-0.081	0.007	0.007
0.805	0.421	-0.424	0.202	-0.059	0.010	0.010
0.814	0.435	-0.403	0.216	-0.038	0.009	0.008
0.838	0.503	-0.456	0.284	-0.091	0.006	0.006
0.840	0.411	-0.410	0.192	-0.045	0.007	0.007
0.844	0.376	-0.425	0.157	-0.060	0.008	0.009
0.852	0.391	-0.432	0.172	-0.067	0.011	0.011
0.863	0.435	-0.357	0.216	0.008	0.009	0.008
0.872	0.451	-0.640	0.232	-0.275	0.011	0.010
0.873	0.467	-0.437	0.248	-0.072	0.012	0.011
0.878	0.374	-0.388	0.155	-0.023	0.009	0.009
0.883	0.389	-0.397	0.170	-0.032	0.007	0.008
0.888	0.308	-0.376	0.089	-0.011	0.006	0.007
0.892	0.376	-0.396	0.157	-0.031	0.010	0.011
0.907	0.468	-0.442	0.249	-0.077	0.011	0.011
0.922	0.451	-0.407	0.232	-0.042	0.008	0.008
0.941	0.547	-0.396	0.328	-0.031	0.013	0.010
0.949	0.540	-0.490	0.321	-0.125	0.010	0.009
0.989	0.558	-0.509	0.339	-0.144	0.016	0.015
0.994	0.623	-0.496	0.404	-0.131	0.016	0.013
0.999	0.514	-0.603	0.295	-0.238	0.012	0.014

Table 5. FCO R Filter Data

Phase	% Q	% U	ISP sub % Q	ISP sub % U	Internal Error % Q	Internal Error % U
0.081	0.318	-0.373	0.131	-0.077	0.007	0.008
0.105	0.454	-0.432	0.267	-0.136	0.011	0.011
0.308	0.503	-0.431	0.316	-0.135	0.008	0.007
0.352	0.376	-0.374	0.189	-0.078	0.012	0.012
0.366	0.504	-0.489	0.317	-0.193	0.018	0.017
0.448	0.261	-0.267	0.074	0.029	0.006	0.007
0.583	0.377	-0.450	0.190	-0.154	0.009	0.011
0.632	0.412	-0.443	0.225	-0.147	0.013	0.014
0.704	0.830	-0.779	0.643	-0.483	0.017	0.016
0.753	0.452	-0.417	0.265	-0.121	0.014	0.013
0.772	0.398	-0.398	0.211	-0.102	0.009	0.009
0.840	0.359	-0.373	0.172	-0.077	0.009	0.004
0.844	0.330	-0.372	0.143	-0.076	0.007	0.007
0.907	0.391	-0.443	0.204	-0.147	0.012	0.021
0.989	0.449	-0.417	0.262	-0.121	0.011	0.010
0.994	0.524	-0.438	0.337	-0.142	0.017	0.015
0.999	0.463	-0.522	0.276	-0.226	0.013	0.014

Table 6. HPOL Synthetic B Filter Data

Phase	% Q	% U	ISP sub % Q	ISP sub % U	Internal Error (%)	Systematic Error (%)
<i>B</i> Band Reticon:						
0.000	0.4323	-0.6592	0.2020	-0.2953	0.0019	0.0200
0.121	0.3905	-0.4928	0.1603	-0.1289	0.0030	0.0200
0.206	0.4691	-0.4456	0.2388	-0.0816	0.0062	0.0200
0.292	0.4248	-0.5536	0.1945	-0.1897	0.0015	0.0200
0.358	0.4874	-0.4409	0.2572	-0.0770	0.0023	0.0200
0.368	0.4823	-0.4503	0.2521	-0.0864	0.0016	0.0200
0.525	0.2897	-0.4828	0.0594	-0.1188	0.0034	0.0200
0.657	0.5574	-0.5334	0.3272	-0.1695	0.0030	0.0200
0.661	0.5392	-0.5076	0.3090	-0.1436	0.0023	0.0200
0.668	0.5611	-0.5302	0.3308	-0.1663	0.0015	0.0200
0.737	0.4881	-0.5021	0.2578	-0.1382	0.0019	0.0200
0.762	0.4841	-0.5642	0.2538	-0.2003	0.0011	0.0200
0.890	0.4337	-0.4554	0.2027	-0.0953	0.0033	0.0200
0.962	0.5317	-0.6448	0.3015	-0.2810	0.0019	0.0200
<i>B</i> Band CCD:						
0.000	0.3794	-0.8971	0.1492	-0.5332	0.0044	0.0220
0.004	0.5419	-0.4592	0.3117	-0.0953	0.0031	0.0220
0.008	0.3222	-0.8462	0.0920	-0.4823	0.0046	0.0220
0.010	0.4679	-0.4787	0.2377	-0.1149	0.0063	0.0220
0.011	0.4846	-0.5516	0.2544	-0.1877	0.0035	0.0220
0.015	0.2608	-0.8606	0.0326	-0.4982	0.0082	0.0220
0.019	0.3952	-0.5281	0.1650	-0.1643	0.0053	0.0220
0.039	0.3981	-0.6422	0.1679	-0.2783	0.0030	0.0100
0.043	0.6360	-0.5666	0.4058	-0.2028	0.0034	0.0100
0.069	0.4896	-0.5155	0.2594	-0.1516	0.0036	0.0140
0.073	0.3301	-0.3861	0.0999	-0.0223	0.0024	0.0140
0.079	0.3372	-0.5482	0.1070	-0.1843	0.0029	0.0220
0.086	0.2982	-0.3927	0.0680	-0.0289	0.0033	0.0220
0.087	0.3415	-0.5013	0.1113	-0.1374	0.0029	0.0220
0.117	0.3875	-0.4219	0.1573	-0.0581	0.0023	0.0100
0.145	0.3608	-0.4670	0.1307	-0.1030	0.0027	0.0140
0.184	0.2940	-0.4482	0.0638	-0.0844	0.0027	0.0100
0.219	0.4525	-0.5404	0.2223	-0.1765	0.0028	0.0140
0.226	0.4000	-0.5080	0.1698	-0.1442	0.0024	0.0140
0.283	0.4840	-0.6685	0.2538	-0.3047	0.0018	0.0140
0.287	0.3671	-0.5343	0.1368	-0.1704	0.0028	0.0150
0.300	0.3961	-0.6073	0.1659	-0.2435	0.0054	0.0150
0.333	0.5179	-0.5637	0.2877	-0.1998	0.0025	0.0080
0.354	0.4517	-0.5322	0.2215	-0.1683	0.0025	0.0150
0.385	0.4775	-0.5832	0.2473	-0.2193	0.0031	0.0220
0.401	0.3079	-0.4730	0.0777	-0.1091	0.0029	0.0220
0.403	0.3754	-0.4673	0.1453	-0.1027	0.0057	0.0220
0.410	0.3475	-0.3311	0.1174	0.0327	0.0024	0.0100
0.447	0.2957	-0.3379	0.0655	0.0261	0.0025	0.0140
0.455	0.3165	-0.3542	0.0863	0.0097	0.0028	0.0140

Table 6—Continued

Phase	% Q	% U	ISP sub % Q	ISP sub % U	Internal Error (%)	Systematic Error (%)
0.463	0.3221	-0.4072	0.0920	-0.0433	0.0047	0.0140
0.483	0.4778	-0.4378	0.2475	-0.0739	0.0020	0.0300
0.485	0.3250	-0.3518	0.0948	0.0121	0.0022	0.0100
0.486	0.3433	-0.4030	0.1131	-0.0391	0.0041	0.0220
0.525	0.3457	-0.5121	0.1155	-0.1482	0.0029	0.0140
0.534	0.3062	-0.5369	0.0760	-0.1730	0.0099	0.0140
0.572	0.4309	-0.4738	0.2006	-0.1099	0.0020	0.0100
0.645	0.4821	-0.5407	0.2519	-0.1769	0.0050	0.0220
0.671	0.5691	-0.5555	0.3388	-0.1916	0.0024	0.0150
0.723	0.5293	-0.6009	0.2990	-0.2369	0.0051	0.0080
0.749	0.5268	-0.4740	0.2965	-0.1101	0.0020	0.0100
0.796	0.4758	-0.5419	0.2455	-0.1780	0.0017	0.0100
0.833	0.3884	-0.5293	0.1581	-0.1654	0.0024	0.0140
0.842	0.3740	-0.5620	0.1438	-0.1981	0.0026	0.0140
0.848	0.4561	-0.5198	0.2259	-0.1559	0.0033	0.0100
0.848	0.3216	-0.5164	0.0914	-0.1526	0.0025	0.0140
0.862	0.4337	-0.4914	0.2035	-0.1276	0.0023	0.0100
0.912	0.3993	-0.4460	0.1691	-0.0821	0.0024	0.0140
0.920	0.4319	-0.4887	0.2017	-0.1249	0.0041	0.0140
0.939	0.5136	-0.7251	0.2834	-0.3612	0.0035	0.0220
0.955	0.7422	-0.5796	0.5120	-0.2158	0.0051	0.0100
0.969	0.6624	-0.5345	0.4322	-0.1707	0.0041	0.0100
0.980	0.4666	-0.7196	0.2365	-0.3557	0.0082	0.0140

Table 7. HPOL Synthetic V Filter Data

Phase	% Q	% U	ISP sub % Q	ISP sub % U	Internal Error (%)	Systematic Error (%)
V Band Reticon:						
0.121	0.3620	-0.4839	0.1427	-0.1373	0.0025	0.0200
0.206	0.4578	-0.3863	0.2386	-0.0398	0.0056	0.0200
0.292	0.4058	-0.5298	0.1865	-0.1830	0.0018	0.0200
0.358	0.4499	-0.4464	0.2306	-0.0998	0.0024	0.0200
0.368	0.4474	-0.4376	0.2280	-0.0909	0.0020	0.0200
0.525	0.2534	-0.4453	0.0339	-0.0985	0.0026	0.0200
0.657	0.5430	-0.4910	0.3236	-0.1444	0.0032	0.0200
0.661	0.4934	-0.4758	0.2741	-0.1291	0.0021	0.0200
0.668	0.5306	-0.4902	0.3113	-0.1435	0.0017	0.0200
0.737	0.4451	-0.4905	0.2258	-0.1438	0.0018	0.0200
0.762	0.4531	-0.5427	0.2337	-0.1960	0.0013	0.0200
0.890	0.3825	-0.4272	0.1590	-0.0808	0.0053	0.0200
0.962	0.5339	-0.6376	0.3147	-0.2910	0.0023	0.0200
V Band CCD:						
0.000	0.3923	-0.7974	0.1732	-0.4508	0.0029	0.0100
0.004	0.5482	-0.4414	0.3288	-0.0948	0.0020	0.0100
0.008	0.3562	-0.7982	0.1370	-0.4516	0.0030	0.0100
0.010	0.5082	-0.4602	0.2892	-0.1139	0.0037	0.0100
0.011	0.5266	-0.5742	0.3075	-0.2280	0.0022	0.0100
0.015	0.3205	-0.8314	0.1022	-0.4861	0.0044	0.0100
0.019	0.4657	-0.5516	0.2464	-0.2053	0.0029	0.0100
0.039	0.4228	-0.6091	0.2038	-0.2631	0.0021	0.0050
0.043	0.6145	-0.5334	0.3948	-0.1860	0.0024	0.0050
0.069	0.4805	-0.5109	0.2612	-0.1644	0.0024	0.0070
0.073	0.3706	-0.3841	0.1516	-0.0382	0.0016	0.0070
0.079	0.3369	-0.5427	0.1179	-0.1966	0.0018	0.0100
0.086	0.3240	-0.4117	0.1047	-0.0652	0.0021	0.0100
0.087	0.3497	-0.4760	0.1304	-0.1295	0.0018	0.0100
0.117	0.3706	-0.3946	0.1517	-0.0479	0.0015	0.0050
0.145	0.3556	-0.4517	0.1361	-0.1047	0.0019	0.0070
0.184	0.3099	-0.4214	0.0903	-0.0756	0.0017	0.0050
0.219	0.4250	-0.5151	0.2058	-0.1685	0.0019	0.0070
0.226	0.3969	-0.5070	0.1777	-0.1604	0.0016	0.0070
0.283	0.4976	-0.6274	0.2777	-0.2799	0.0012	0.0070
0.287	0.3863	-0.5250	0.1671	-0.1785	0.0017	0.0100
0.300	0.3968	-0.5232	0.1779	-0.1771	0.0030	0.0100
0.333	0.5109	-0.5433	0.2916	-0.1967	0.0016	0.0050
0.354	0.4459	-0.4969	0.2268	-0.1506	0.0016	0.0100
0.385	0.4809	-0.5536	0.2617	-0.2070	0.0019	0.0100
0.401	0.3649	-0.4747	0.1452	-0.1273	0.0019	0.0100
0.403	0.3778	-0.4680	0.1584	-0.1217	0.0032	0.0100
0.410	0.3568	-0.3198	0.1376	0.0266	0.0018	0.0050
0.447	0.3001	-0.3333	0.0811	0.0132	0.0017	0.0070
0.455	0.3256	-0.3258	0.1063	0.0209	0.0018	0.0070
0.463	0.3353	-0.3521	0.1161	-0.0056	0.0031	0.0070

Table 7—Continued

Phase	% Q	% U	ISP sub % Q	ISP sub % U	Internal Error (%)	Systematic Error (%)
0.483	0.4529	-0.4384	0.2338	-0.0928	0.0014	0.0200
0.485	0.3189	-0.3351	0.1000	0.0106	0.0015	0.0050
0.486	0.3571	-0.4099	0.1378	-0.0634	0.0025	0.0100
0.525	0.3109	-0.5088	0.0915	-0.1620	0.0019	0.0070
0.534	0.2687	-0.5048	0.0508	-0.1606	0.0059	0.0070
0.559	0.5740	-0.4877	0.3675	-0.1488	0.0045	0.0050
0.572	0.4404	-0.4434	0.2215	-0.0974	0.0014	0.0050
0.645	0.4919	-0.5245	0.2736	-0.1783	0.0027	0.0100
0.653	0.6036	-0.4925	0.3022	-0.1452	0.0022	0.0050
0.671	0.5323	-0.5334	0.3130	-0.1869	0.0015	0.0100
0.723	0.4912	-0.5611	0.2714	-0.2138	0.0034	0.0050
0.749	0.5054	-0.4378	0.2861	-0.0908	0.0013	0.0050
0.796	0.4662	-0.5150	0.2471	-0.1688	0.0012	0.0050
0.833	0.3579	-0.5014	0.1386	-0.1549	0.0017	0.0070
0.842	0.3457	-0.5039	0.1264	-0.1573	0.0018	0.0070
0.848	0.4292	-0.4756	0.2104	-0.1292	0.0020	0.0050
0.848	0.3131	-0.4951	0.0939	-0.1483	0.0016	0.0070
0.862	0.4222	-0.4591	0.2037	-0.1134	0.0015	0.0050
0.912	0.3943	-0.4385	0.1748	-0.0918	0.0016	0.0070
0.920	0.3880	-0.4313	0.1690	-0.0849	0.0025	0.0070
0.939	0.4909	-0.6709	0.2715	-0.3242	0.0022	0.0100
0.955	0.6986	-0.5220	0.4790	-0.1747	0.0035	0.0050
0.969	0.6168	-0.4929	0.3989	-0.1476	0.0028	0.0050
0.980	0.4644	-0.5950	0.2447	-0.2476	0.0053	0.0070

Table 8. HPOL Synthetic R Filter Data

Phase	% Q	% U	ISP sub % Q	ISP sub % U	Internal Error (%)	Systematic Error (%)
<i>R</i> Band Reticon:						
0.000	0.4242	-0.5664	0.2205	-0.2422	0.0027	0.0200
0.121	0.3360	-0.4694	0.1341	-0.1494	0.0038	0.0200
0.206	0.3777	-0.3521	0.1861	-0.0332	0.0067	0.0200
0.292	0.3735	-0.4713	0.1709	-0.1498	0.0025	0.0200
0.358	0.3955	-0.4077	0.1947	-0.0863	0.0032	0.0200
0.368	0.3917	-0.4168	0.1852	-0.0923	0.0027	0.0200
0.525	0.2297	-0.4119	0.0295	-0.0905	0.0032	0.0200
0.657	0.4936	-0.4751	0.2912	-0.1619	0.0045	0.0200
0.661	0.4402	-0.4586	0.2373	-0.1349	0.0033	0.0200
0.668	0.4711	-0.4491	0.2711	-0.1300	0.0022	0.0200
0.737	0.3817	-0.4389	0.1567	-0.1187	0.0042	0.0200
0.762	0.4064	-0.4960	0.2035	-0.1761	0.0018	0.0200
0.890	0.2308	-0.5012	0.0096	-0.1950	0.0098	0.0200
0.962	0.4678	-0.5736	0.2714	-0.2479	0.0035	0.0200
<i>R</i> Band CCD:						
0.000	0.4015	-0.6876	0.1993	-0.3676	0.0020	0.0080
0.004	0.5123	-0.4037	0.3090	-0.0828	0.0014	0.0080
0.008	0.3668	-0.7072	0.1640	-0.3878	0.0019	0.0080
0.010	0.4717	-0.3918	0.2708	-0.0742	0.0019	0.0080
0.011	0.5048	-0.5398	0.3034	-0.2217	0.0014	0.0080
0.015	0.3437	-0.7394	0.1418	-0.4221	0.0036	0.0080
0.019	0.4562	-0.5390	0.2541	-0.2205	0.0017	0.0080
0.039	0.4169	-0.5498	0.2151	-0.2291	0.0014	0.0040
0.043	0.5921	-0.5174	0.3832	-0.1864	0.0025	0.0040
0.069	0.4405	-0.4660	0.2384	-0.1469	0.0015	0.0070
0.073	0.3695	-0.3606	0.1678	-0.0419	0.0010	0.0070
0.079	0.3101	-0.5081	0.1085	-0.1898	0.0011	0.0080
0.086	0.3175	-0.4057	0.1147	-0.0859	0.0013	0.0080
0.087	0.3317	-0.4421	0.1289	-0.1217	0.0012	0.0080
0.117	0.3510	-0.3731	0.1492	-0.0526	0.0010	0.0040
0.145	0.3317	-0.4227	0.1267	-0.0989	0.0015	0.0070
0.184	0.2922	-0.3812	0.0882	-0.0616	0.0011	0.0040
0.219	0.3710	-0.4600	0.1691	-0.1402	0.0012	0.0070
0.226	0.3663	-0.4598	0.1638	-0.1391	0.0011	0.0070
0.283	0.4810	-0.5997	0.2692	-0.2653	0.0015	0.0070
0.287	0.3534	-0.4673	0.1512	-0.1477	0.0011	0.0140
0.300	0.3697	-0.4742	0.1683	-0.1560	0.0018	0.0140
0.333	0.4735	-0.4876	0.2710	-0.1675	0.0010	0.0080
0.354	0.4001	-0.4492	0.1984	-0.1304	0.0010	0.0140
0.385	0.4323	-0.4968	0.2300	-0.1768	0.0012	0.0080
0.401	0.3302	-0.4507	0.1257	-0.1271	0.0015	0.0080
0.403	0.3535	-0.4378	0.1509	-0.1187	0.0020	0.0080
0.410	0.3238	-0.2942	0.1197	0.0269	0.0012	0.0040
0.447	0.2888	-0.3107	0.0874	0.0085	0.0011	0.0070
0.455	0.3009	-0.3000	0.0987	0.0201	0.0011	0.0070

Table 8—Continued

Phase	% Q	% U	ISP sub % Q	ISP sub % U	Internal Error (%)	Systematic Error (%)
0.463	0.3125	-0.3099	0.1106	0.0090	0.0017	0.0070
0.483	0.4170	-0.3947	0.2131	-0.0749	0.0009	0.0200
0.485	0.2997	-0.2970	0.0976	0.0219	0.0010	0.0040
0.486	0.3217	-0.3832	0.1196	-0.0638	0.0014	0.0080
0.525	0.3155	-0.4577	0.1120	-0.1365	0.0014	0.0070
0.534	0.2685	-0.4502	0.0701	-0.1377	0.0016	0.0070
0.559	0.5560	-0.4658	0.3583	-0.1510	0.0022	0.0040
0.572	0.4179	-0.3970	0.2160	-0.0770	0.0009	0.0040
0.645	0.4237	-0.4673	0.2253	-0.1500	0.0015	0.0080
0.653	0.4946	-0.4361	0.2744	-0.1159	0.0011	0.0040
0.671	0.4657	-0.4839	0.2640	-0.1650	0.0009	0.0140
0.723	0.4251	-0.5203	0.2193	-0.1945	0.0028	0.0080
0.749	0.4687	-0.4084	0.2651	-0.0870	0.0009	0.0040
0.796	0.4310	-0.4647	0.2274	-0.1439	0.0008	0.0040
0.833	0.3140	-0.4453	0.1120	-0.1262	0.0010	0.0070
0.842	0.2980	-0.4499	0.0959	-0.1305	0.0011	0.0070
0.848	0.3819	-0.4402	0.1778	-0.1185	0.0014	0.0040
0.848	0.2874	-0.4334	0.0851	-0.1131	0.0012	0.0070
0.862	0.3860	-0.4130	0.1842	-0.0936	0.0010	0.0040
0.912	0.3574	-0.3987	0.1543	-0.0783	0.0011	0.0070
0.920	0.3495	-0.3898	0.1483	-0.0707	0.0014	0.0070
0.939	0.4245	-0.5886	0.2219	-0.2686	0.0015	0.0080
0.955	0.6552	-0.4704	0.4477	-0.1407	0.0039	0.0040
0.969	0.5424	-0.4346	0.3401	-0.1159	0.0016	0.0040
0.980	0.4749	-0.5607	0.2626	-0.2252	0.0059	0.0070

Table 9. HPOL Synthetic *I* Filter Data

Phase	% <i>Q</i>	% <i>U</i>	ISP sub % <i>Q</i>	ISP sub % <i>U</i>	Internal Error (%)	Systematic Error (%)
<i>I</i> Band Reticon:						
0.000	0.3626	-0.5178	0.1859	-0.1806	0.0107	0.0200
0.121	0.3121	-0.5255	0.1643	-0.2718	0.0210	0.0200
0.206	0.2211	-0.3197	0.2852	-0.0712	0.0212	0.0200
0.292	0.2800	-0.4636	0.1333	-0.1712	0.0147	0.0200
0.358	0.2809	-0.3208	0.1720	-0.0486	0.0135	0.0200
0.368	0.3388	-0.4346	0.1126	-0.0753	0.0167	0.0200
0.525	0.2337	-0.3604	0.1426	-0.1002	0.0127	0.0200
0.657	0.4512	-0.4725	0.2977	-0.3356	0.0278	0.0200
0.661	0.3869	-0.4243	0.2265	-0.0991	0.0178	0.0200
0.668	0.4397	-0.3904	0.3286	-0.1580	0.0090	0.0200
0.737	0.2630	-0.2777	-0.2879	-0.0631	0.0139	0.0200
0.762	0.3384	-0.4473	0.1821	-0.1987	0.0061	0.0200
0.890	-0.3013	-0.9340	-0.4458	-0.6993	0.0649	0.0200
0.962	0.4211	-0.5398	0.3808	-0.1714	0.0138	0.0200
<i>I</i> Band CCD:						
0.000	0.3804	-0.5442	0.2091	-0.2734	0.0019	0.0080
0.004	0.4507	-0.3146	0.2795	-0.0439	0.0014	0.0080
0.008	0.3583	-0.5498	0.1870	-0.2790	0.0018	0.0080
0.010	0.4507	-0.3272	0.2794	-0.0564	0.0018	0.0080
0.011	0.4749	-0.4690	0.3036	-0.1983	0.0014	0.0080
0.015	0.3397	-0.5846	0.1683	-0.3138	0.0038	0.0080
0.019	0.4457	-0.4810	0.2744	-0.2102	0.0017	0.0080
0.039	0.3865	-0.4621	0.2152	-0.1913	0.0015	0.0070
0.043	0.5194	-0.4285	0.3481	-0.1578	0.0016	0.0070
0.069	0.3885	-0.3872	0.2171	-0.1163	0.0012	0.0080
0.073	0.3375	-0.3073	0.1662	-0.0366	0.0011	0.0080
0.079	0.2636	-0.4484	0.0923	-0.1777	0.0012	0.0080
0.086	0.2855	-0.3658	0.1142	-0.0951	0.0013	0.0080
0.087	0.2864	-0.3721	0.1150	-0.1013	0.0012	0.0080
0.117	0.2913	-0.3028	0.1198	-0.0321	0.0010	0.0070
0.145	0.2625	-0.3677	0.0912	-0.0968	0.0019	0.0080
0.184	0.2252	-0.2967	0.0538	-0.0259	0.0012	0.0070
0.219	0.2874	-0.3558	0.1159	-0.0849	0.0012	0.0080
0.226	0.2898	-0.3749	0.1183	-0.1040	0.0011	0.0080
0.287	0.2746	-0.3784	0.1034	-0.1078	0.0011	0.0220
0.300	0.2952	-0.4062	0.1240	-0.1356	0.0017	0.0220
0.333	0.3977	-0.4008	0.2263	-0.1298	0.0011	0.0060
0.354	0.3203	-0.3821	0.1489	-0.1112	0.0010	0.0220
0.385	0.3443	-0.3991	0.1731	-0.1284	0.0011	0.0080
0.401	0.2546	-0.3997	0.0833	-0.1289	0.0013	0.0080
0.403	0.2897	-0.3675	0.1184	-0.0967	0.0020	0.0080
0.410	0.2705	-0.2435	0.0991	0.0274	0.0013	0.0070
0.447	0.2618	-0.2654	0.0902	0.0056	0.0012	0.0080
0.455	0.2673	-0.2538	0.0959	0.0171	0.0012	0.0080
0.463	0.2749	-0.2538	0.1035	0.0171	0.0013	0.0080

Table 9—Continued

Phase	% Q	% U	ISP sub % Q	ISP sub % U	Internal Error (%)	Systematic Error (%)
0.483	0.3544	-0.3245	0.1829	-0.0535	0.0010	0.0200
0.485	0.2575	-0.2304	0.0861	0.0405	0.0012	0.0070
0.486	0.2740	-0.3214	0.1030	-0.0509	0.0014	0.0080
0.525	0.3033	-0.3901	0.1319	-0.1192	0.0018	0.0080
0.534	0.2402	-0.3920	0.0689	-0.1213	0.0013	0.0080
0.559	0.5150	-0.4246	0.3438	-0.1540	0.0022	0.0070
0.572	0.3529	-0.3019	0.1815	-0.0309	0.0011	0.0070
0.645	0.3609	-0.3924	0.1897	-0.1218	0.0016	0.0080
0.653	0.3998	-0.3541	0.2285	-0.0833	0.0011	0.0070
0.671	0.3735	-0.4160	0.2021	-0.1452	0.0010	0.0220
0.723	0.2960	-0.4475	0.1246	-0.1766	0.0025	0.0060
0.749	0.3880	-0.3424	0.2166	-0.0715	0.0009	0.0070
0.796	0.3552	-0.3721	0.1839	-0.1013	0.0009	0.0070
0.833	0.2470	-0.3595	0.0756	-0.0886	0.0011	0.0080
0.842	0.2378	-0.3646	0.0665	-0.0937	0.0012	0.0080
0.848	0.2912	-0.3398	0.1198	-0.0689	0.0018	0.0070
0.848	0.2267	-0.3582	0.0553	-0.0873	0.0014	0.0080
0.862	0.3112	-0.3377	0.1400	-0.0670	0.0011	0.0070
0.912	0.3068	-0.3286	0.1354	-0.0577	0.0014	0.0080
0.920	0.2922	-0.3419	0.1210	-0.0712	0.0012	0.0080
0.939	0.3517	-0.4706	0.1803	-0.1997	0.0014	0.0080
0.955	0.5040	-0.3810	0.3327	-0.1102	0.0059	0.0070
0.969	0.4425	-0.3480	0.2715	-0.0772	0.0015	0.0070

Table 10. Position Angle Information for β Lyrae

Band	HPOL Reticon (deg)	HPOL CCD (deg)	AH (deg)	FCO (deg)
<i>B</i>	139.8 ± 3.5	165.0 ± 0.7	169.8 ± 1.7	165.1 ± 0.9
<i>V</i>	147.3 ± 3.0	164.0 ± 0.5	171.8 ± 1.0	163.1 ± 0.4
<i>R</i>	158.4 ± 0.4	158.3 ± 0.4	...	162.2 ± 0.7
<i>I</i>	57.3 ± 3.0	162.7 ± 0.6
Index	158.8 ± 0.6	142.1 ± 1.7
H α	...	47.9 ± 9.7
H β	...	71.1 ± 2.5
He I λ 5876	...	63.8 ± 6.4
He I λ 7065	...	51.0 ± 3.2
He I λ 6679	...	138.2 ± 6.6

Note. — These values were calculated by fitting a line in Q - U space to the data, excluding points between phases 0.475 and 0.525. For the HPOL data, we used systematic errors in both Q and U in the least-squares fit calculation for all bands except the Balmer jump index (the vector difference between the polarization above and below the Balmer jump) and the lines, for which we used the intrinsic errors.

Table 11. *BVRI* Fourier Fit Parameters

Band	Zero Point	Term	Ω	A	ϕ
<i>B</i>	0.250453	1	2.98 ± 0.01	0.122 ± 0.008	0.30 ± 0.01
	...	2	1.00 ± 0.02	0.064 ± 0.008	0.39 ± 0.02
<i>V</i>	0.243776	1	2.98 ± 0.01	0.096 ± 0.005	0.30 ± 0.01
	...	2	1.01 ± 0.03	0.048 ± 0.006	0.34 ± 0.03
<i>R</i>	0.241148	1	3.00 ± 0.01	0.107 ± 0.008	0.32 ± 0.01
	...	2	4.02 ± 0.03	0.052 ± 0.009	0.08 ± 0.03
<i>I</i>	0.195021	1	3.00 ± 0.01	0.093 ± 0.006	0.30 ± 0.01
	...	2	4.01 ± 0.02	0.050 ± 0.006	0.10 ± 0.02

Note. — These parameters describe our Fourier fits to the broadband polarimetric data in the combined HPOL, FCO and AH data sets. See Section 3.1.

Table 12. Broadband Secondary Eclipse Phases and Maximum Hot Spot Size

Band	Phase (P)	Min PA Phase Rot	Max PA Phase Rot	Hot Spot Size in Phase	qf_{DC}	qf_{min}	HS_Q	HS_{PA}	HS_{SM}
<i>B</i>	0.481 ± 0.005	0.448	0.543	0.095	0.186	0.045	$28R_{\odot}$	$33R_{\odot}$	$36R_{\odot}$
<i>V</i>	0.483 ± 0.006	0.396	0.554	0.158	0.184	0.080	$28R_{\odot}$	$55R_{\odot}$	$24R_{\odot}$
<i>R</i>	0.449 ± 0.005	0.448	0.524	0.076	0.171	0.080	$40R_{\odot}$	$26R_{\odot}$	$22R_{\odot}$
<i>I</i>	0.449 ± 0.004	0.448	0.524	0.076	0.140	0.077	$40R_{\odot}$	$26R_{\odot}$	$17R_{\odot}$

Note. — Columns two through six are parameters used in the three hot spot size estimates (see Sections 4.1.1, 4.1.2, and 4.1.3). The last three columns represent the width of the hot spot calculated using our three different estimates (see Section 4.1). All three polarimetric data sets were used in this analysis and the resulting estimates.

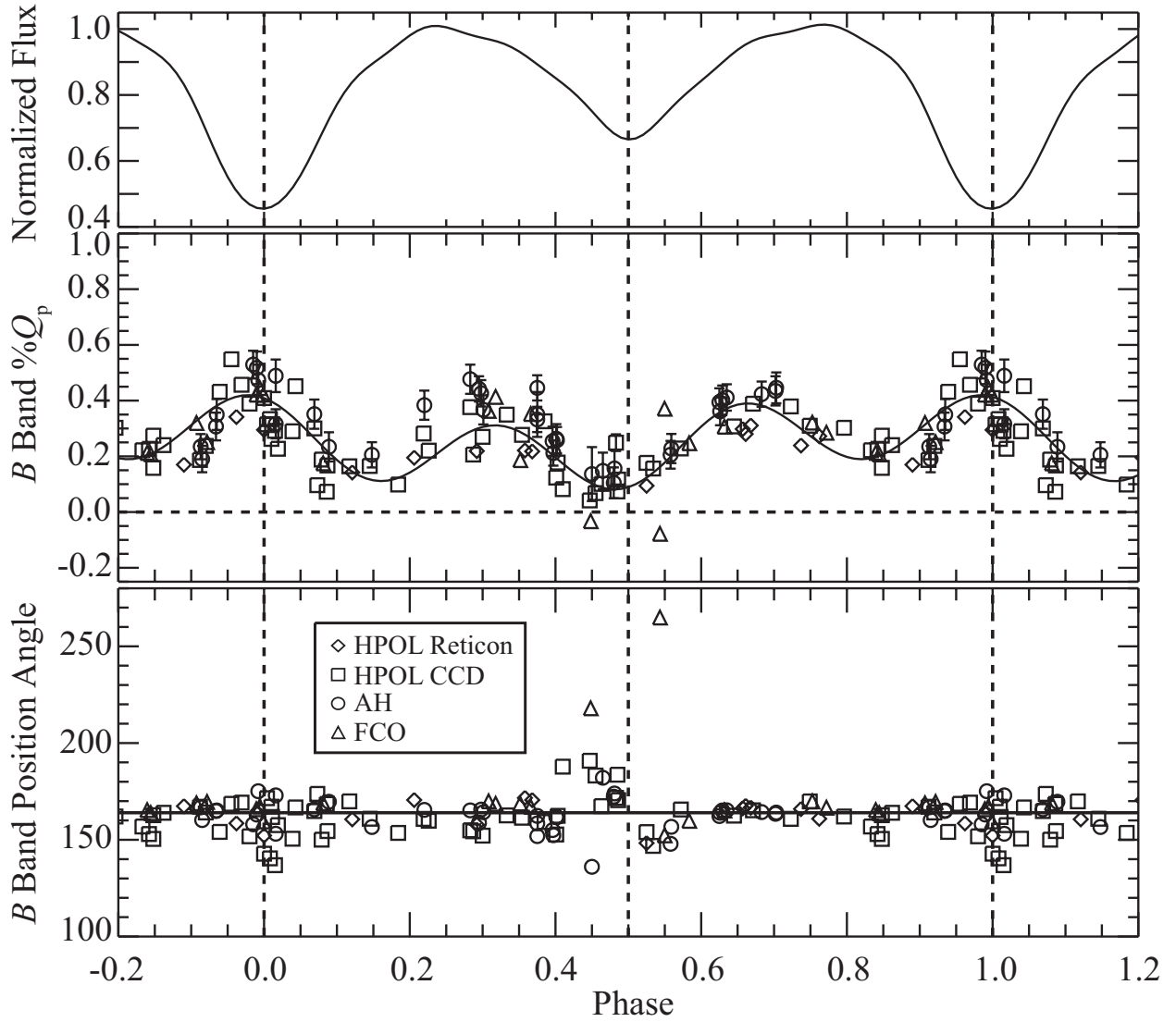


Fig. 1.— Data points represent the B band polarimetric observations from HPOL Reticon (diamonds), HPOL CCD (squares), AH (circles) and FCO (triangles). *From top:* Normalized V band Fourier fit light curve (Harmanec et al. 1996), projected polarization (see Section 3.1), and position angle (degrees) versus phase. Error bars are shown for uncertainties larger than 0.025 in $\%Q_p$ and 5.0° in position angle. The HPOL error bars shown represent the larger of the intrinsic and systematic uncertainties. All data have been wrapped so that more than one complete period is shown. The solid line in the middle panel represents our Fourier fit to the $\%Q_p$ data (see Section 3.1). The dotted line represents zero projected polarization. The solid line in the bottom panel represents the average position angle of 164° .

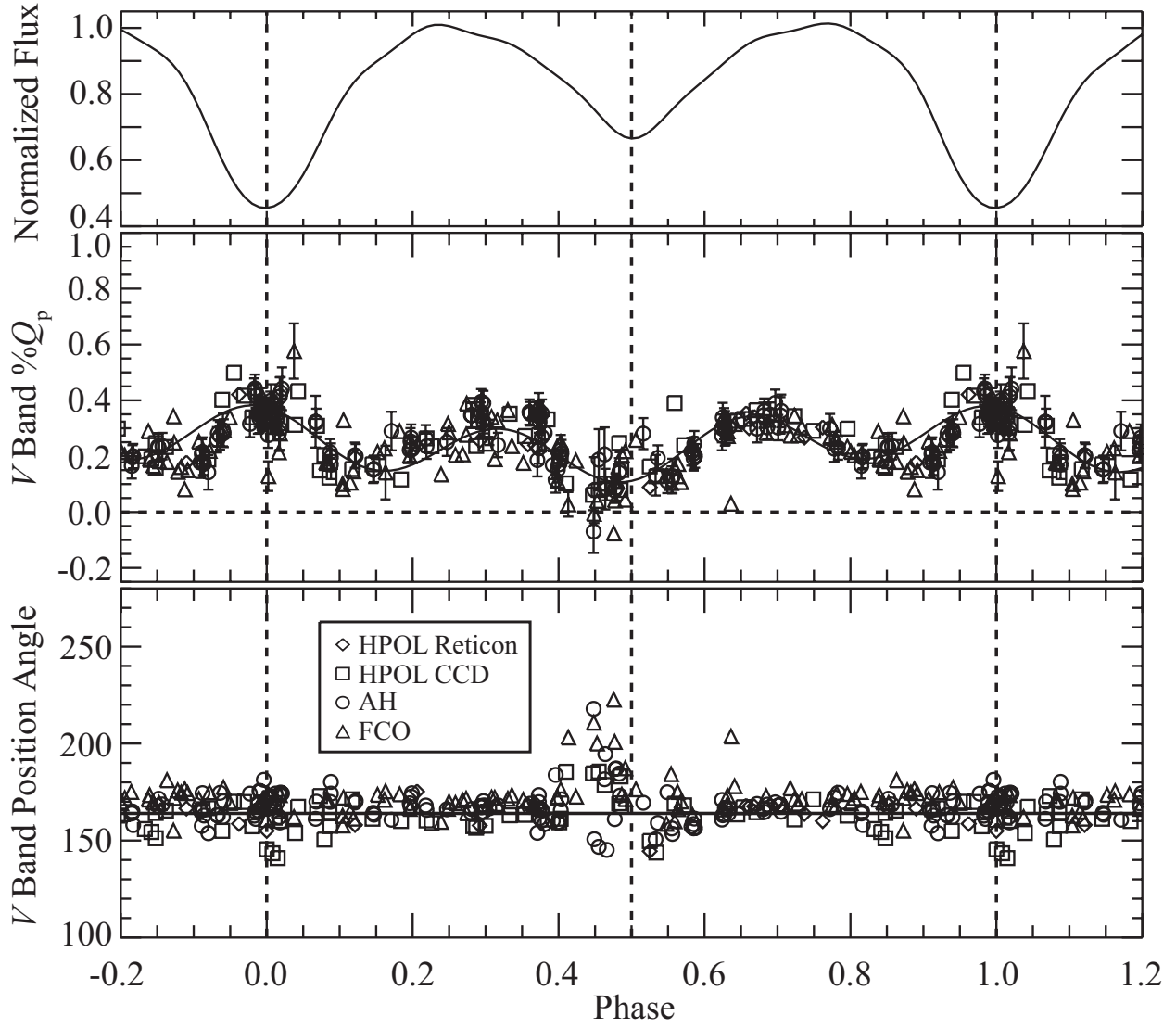


Fig. 2.— Same as Figure 1, but for V band polarimetry.

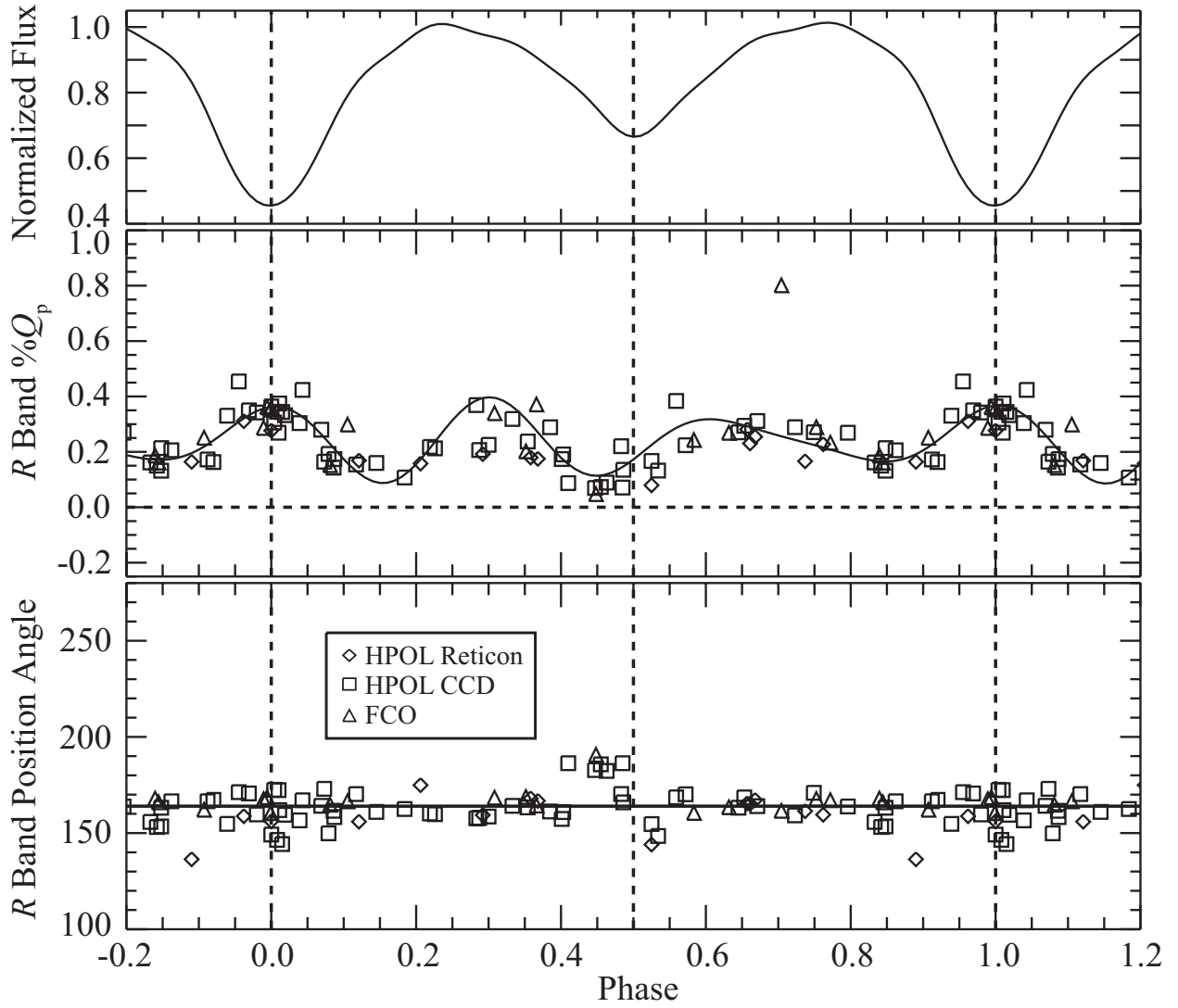


Fig. 3.— Same as Figure 1, but for *R* band polarimetry.

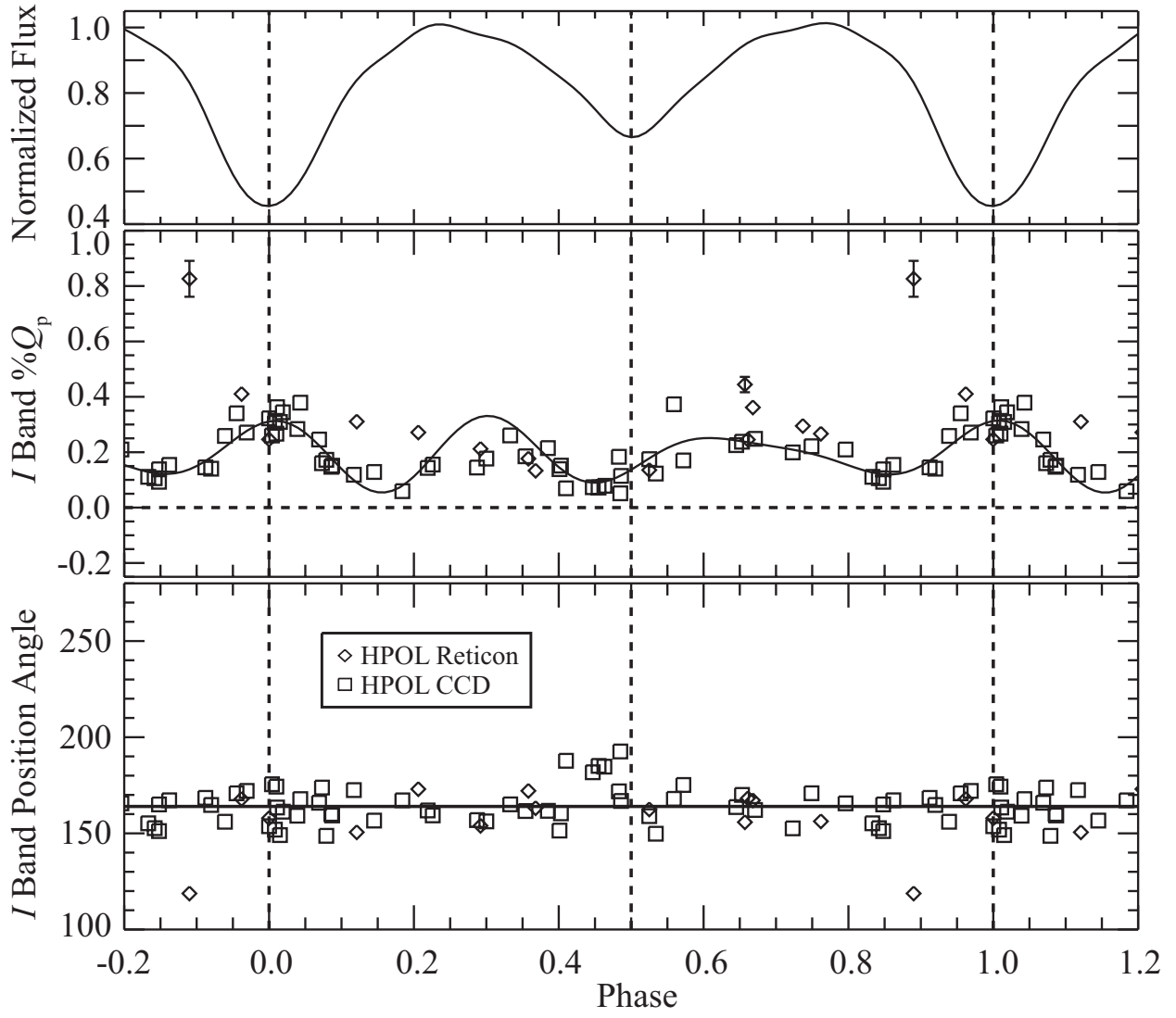


Fig. 4.— Same as Figure 1, but for *I* band polarimetry.

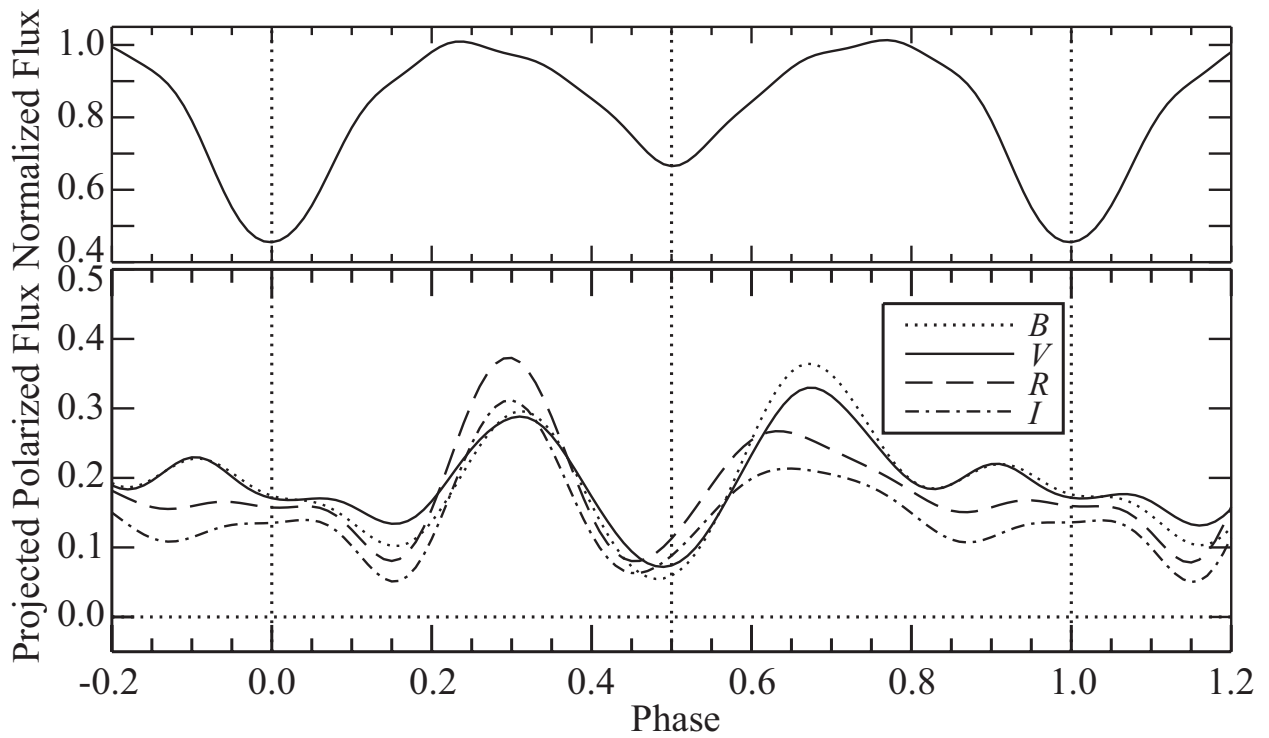


Fig. 5.— *From top:* Normalized V band Fourier fit light curve, projected polarized flux curves for the $BVRI$ bands (see Section 3.1). The projected polarized flux curves are formed by multiplying each band’s Fourier fit polarization curve by its normalized Fourier fit light curve.

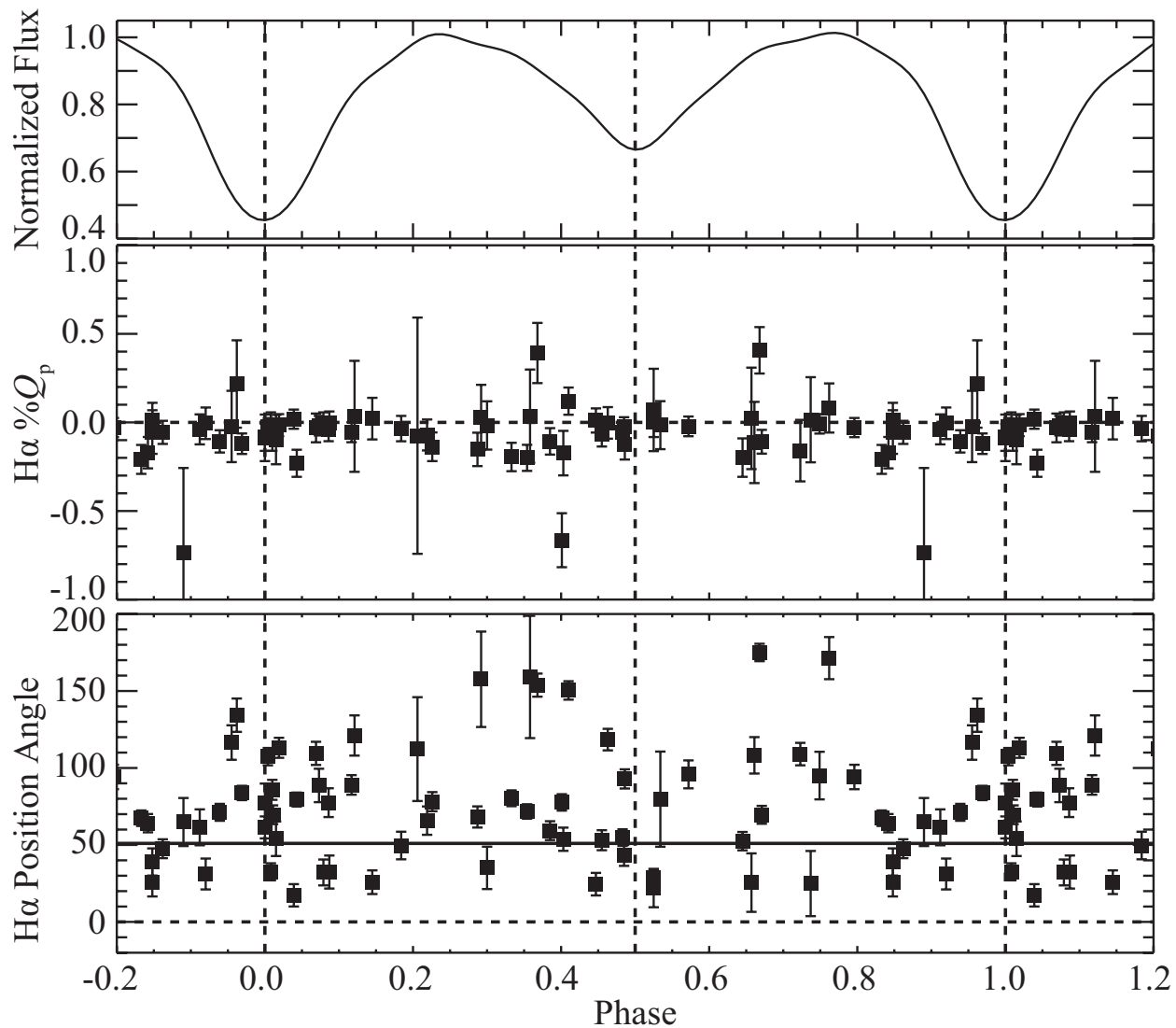


Fig. 6.— $H\alpha$ emission line polarization, corrected for underlying absorption, from HPOL CCD observations (see Section 3.2). *From top:* Normalized V band Fourier fit light curve (Harmanec et al. 1996), projected polarization, and position angle (degrees) versus phase. Error bars represent intrinsic uncertainties. All data have been wrapped in phase to display more than one complete period.

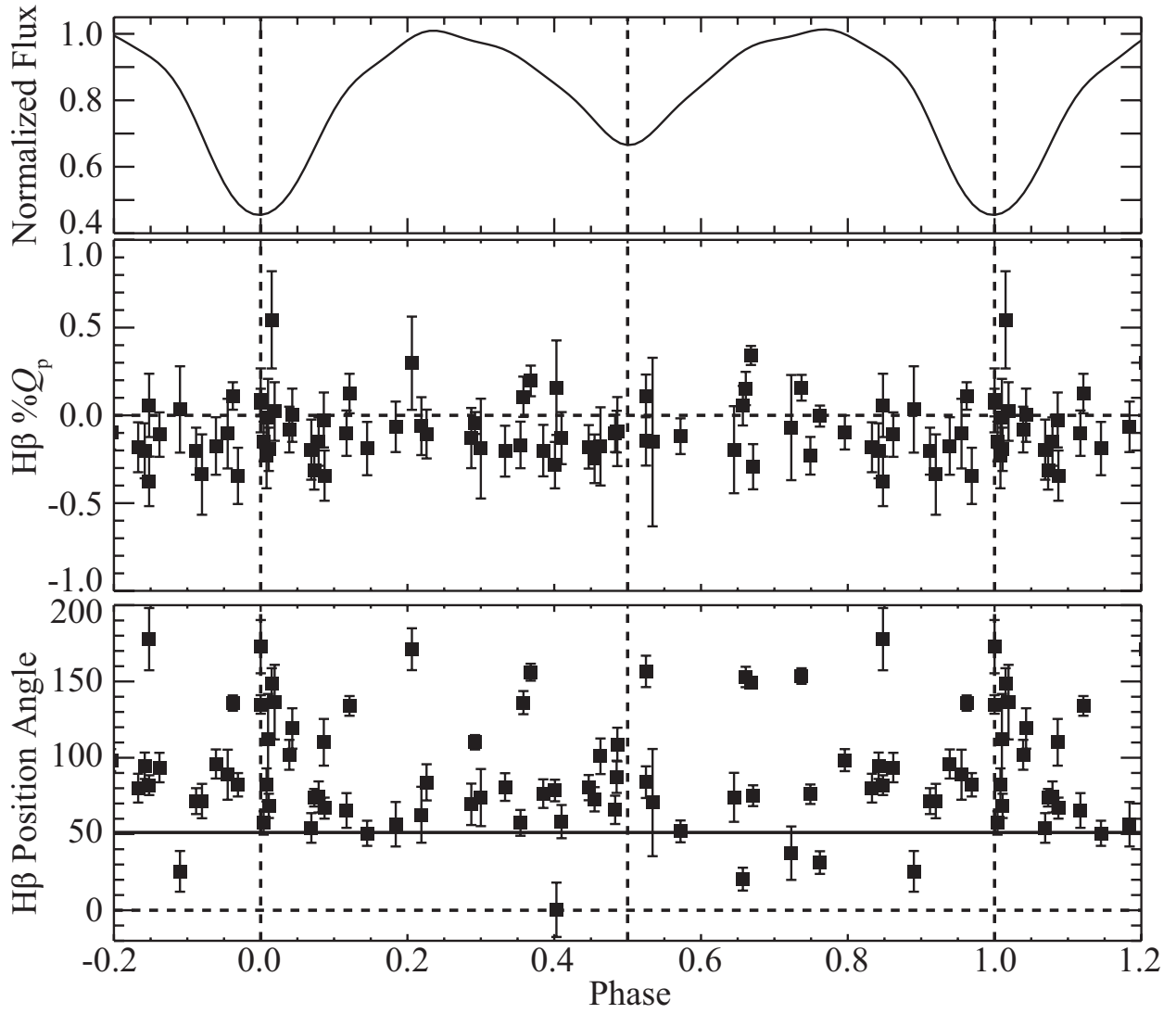


Fig. 7.— Same as Figure 5, but for H β corrected for underlying absorption.

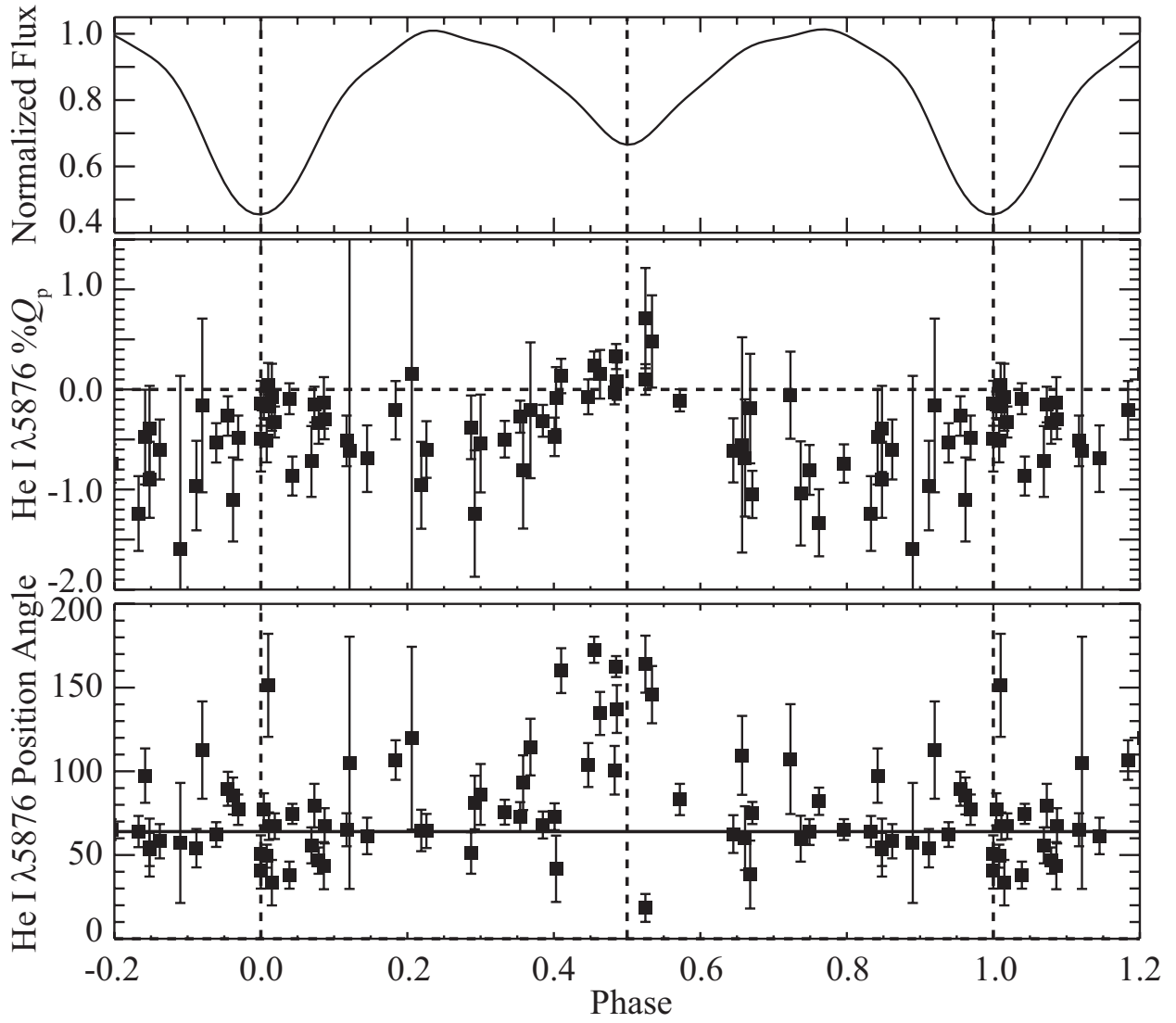


Fig. 8.— Same as Figure 5, but for He I $\lambda 5876$.

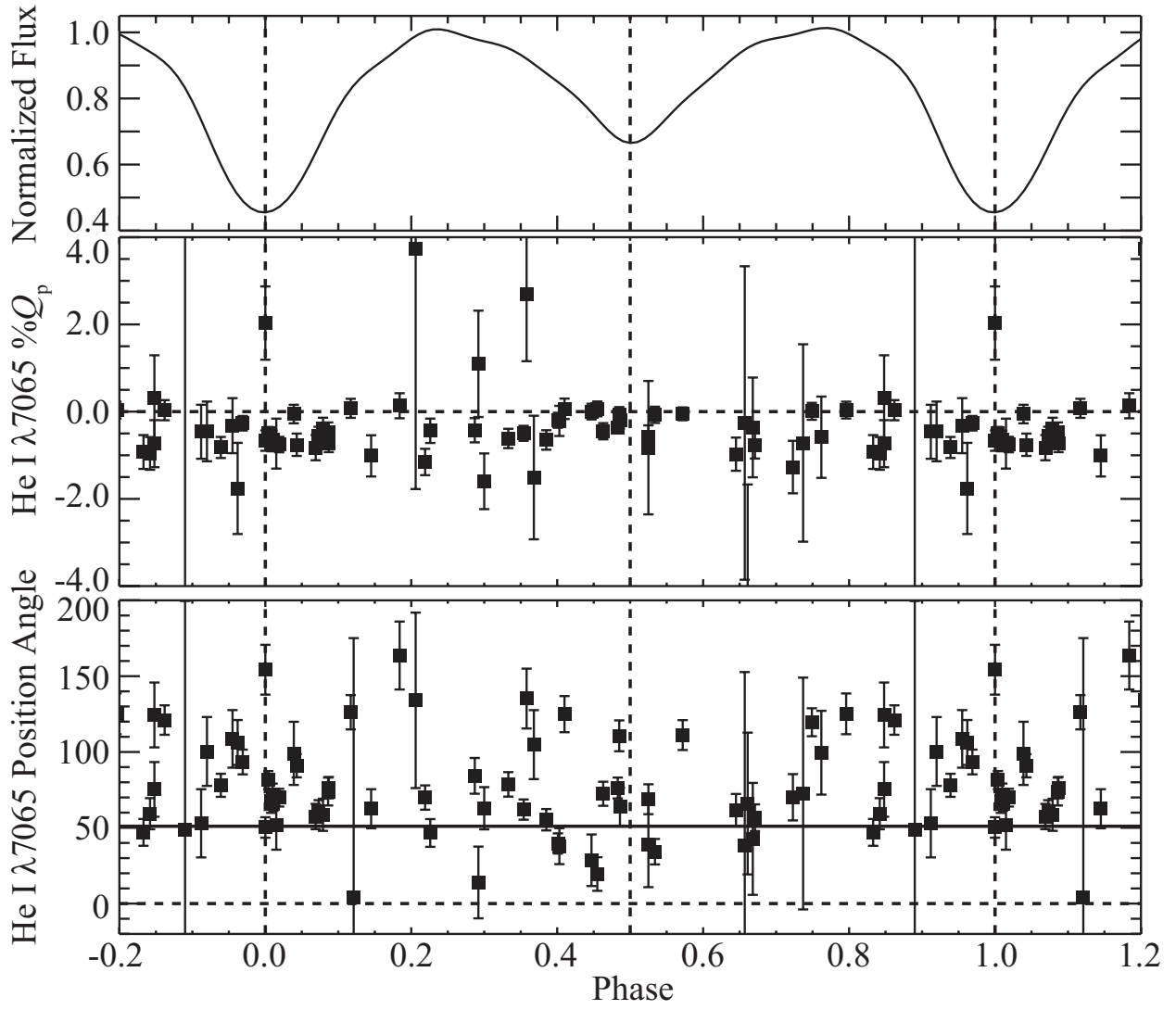


Fig. 9.— Same as Figure 5, but for He I $\lambda 7065$.

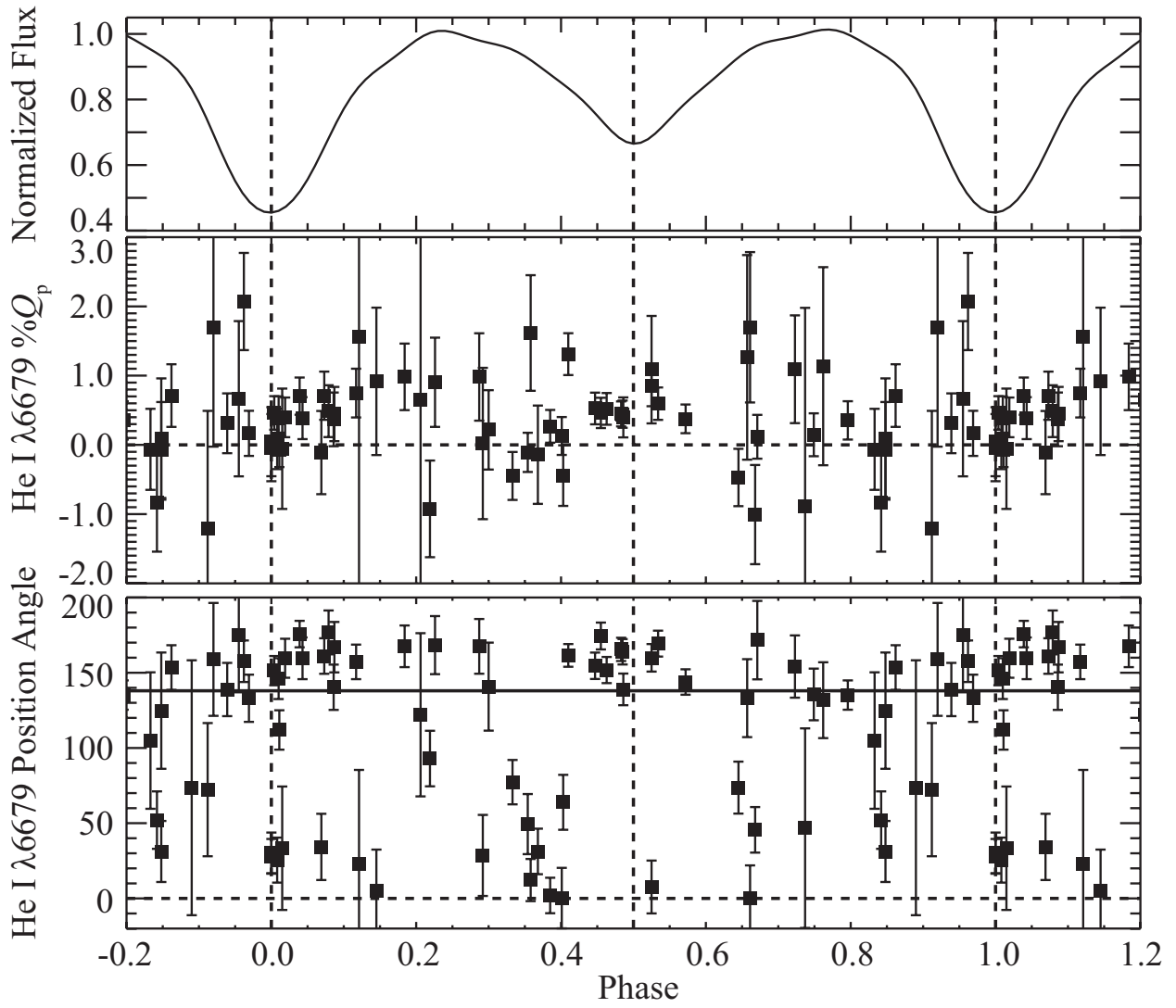


Fig. 10.— Same as Figure 5, but for He I $\lambda 6679$.

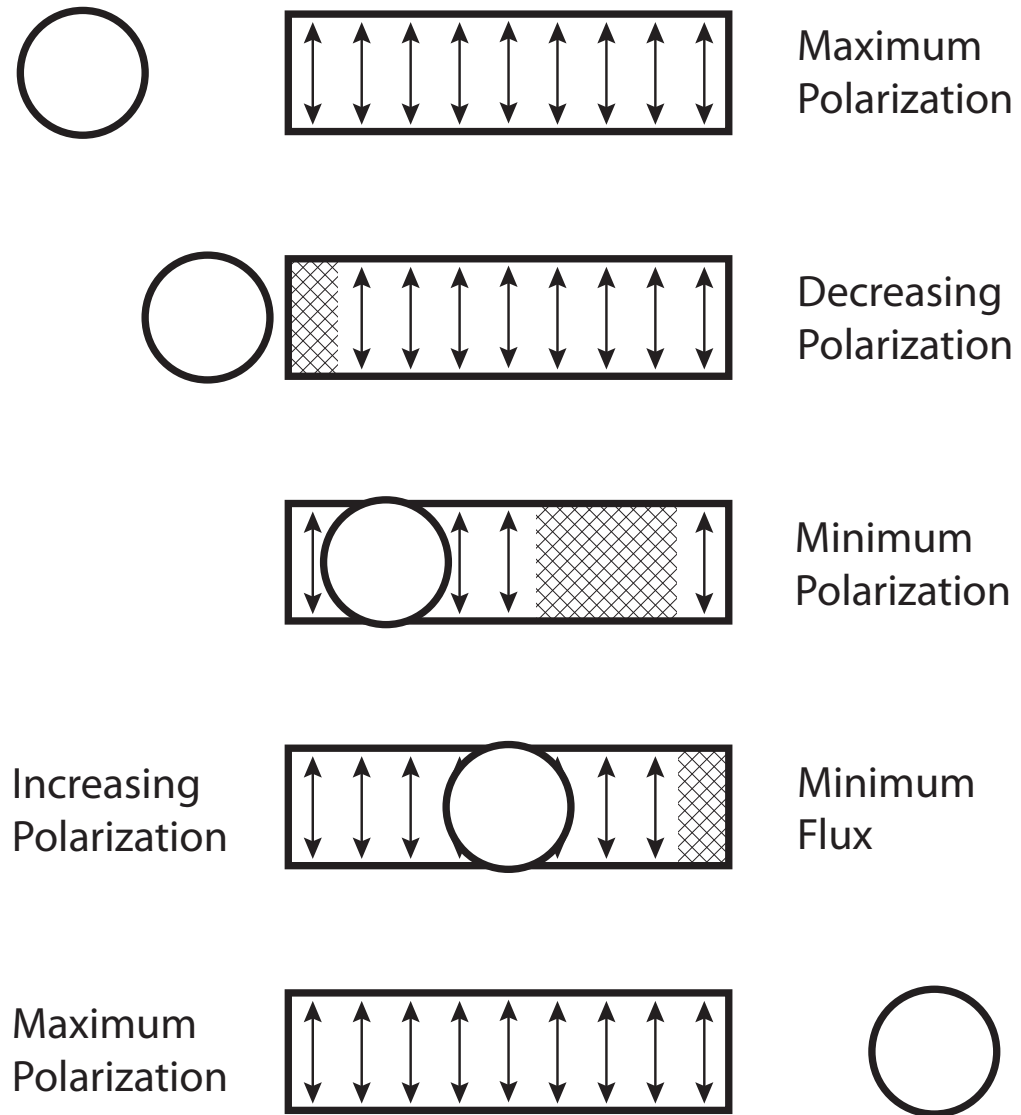


Fig. 11.— Proposed geometry of the β Lyr system at various phases in our proposed hot spot model. Arrows represent the polarization arising from the disk edge. *From Top:* The first maximum in polarization occurs at the first quadrature phase. The polarization then begins to decrease as the hot spot (hatched region) rotates into view. The minimum in polarization occurs when the area eclipsed by the loser and disrupted by the hot spot is maximized. The minimum in flux occurs as the hot spot is rotating off the edge of the visible disk. The second maximum in polarization occurs at the second quadrature phase.

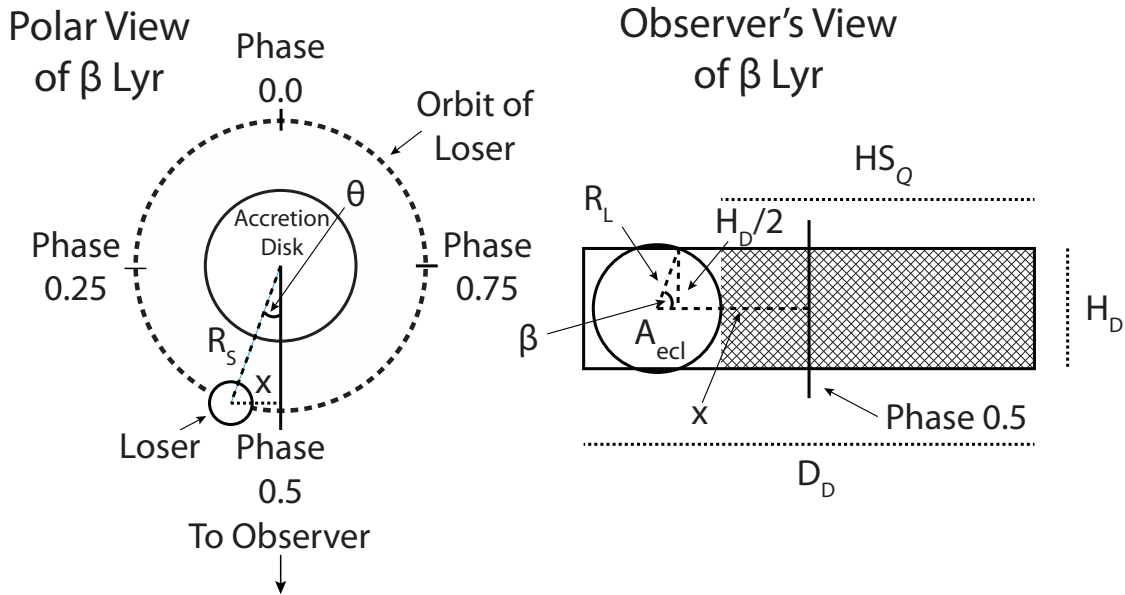


Fig. 12.— Sketch of the geometry we used for our hot spot size estimates (see Section 4.1). We used parameters obtained by Linnell (2000) for the disk height, disk diameter, loser radius and separation between the two components. The hatched region in the Observer’s View represents the hot spot size based on the $\%Q_p$ method (see Section 4.1.1). The blackened area of the circle in the Observer’s View is the unclipped area of the loser at primary eclipse.